APPROXIMATE MODELS FOR NEUTRAL PARTICLE TRANSPORT IN DUCTS WITH WALL MIGRATION

A Dissertation

by

ARNULFO GONZALEZ

Submitted to the Office of Graduate and Professional Studies of
Texas A&M University
in partial fulfillment of the requirements for the degree of

DOCTOR OF PHILOSOPHY

Chair of Committee,	John R. Ford
Co-Chair of Committee,	Ryan G. McClarren
Committee Members,	Sunil S. Chirayath
	John C. Keyser
Head of Department,	Yassin A. Hassan

August 2016

Major Subject: Nuclear Engineering

ABSTRACT

The problem of monoenergetic neutral particle transport in a duct with wall migration for various shielding materials is treated using an approximate one-dimensional model and a Monte Carlo-based multivariate logistic regression model. The one-dimensional model is a third-order approximation in a hierarchy of approximations derived by a weighted residual procedure that accounts for wall migration by means of a kernel density. Physical constants required for the one-dimensional model— scattering probability (c) and the average distance traveled in walls (d)— are calculated using MCNP's PTRAC and a corresponding parsing code. Numerical results for the one-dimensional model are based on a discrete ordinates solution and compared to MCNP. The logistic regression models are developed using the R language in statistical computing for three explanatory variables— duct radius (r), length (L), and shield thickness plus inner radius (S)— where each parameter is explored via univariate models. Data for the models is collected from MCNP via automated processes using Python and shell scripts. The logistic regression models lead to analytical expressions, which are evaluated by randomly dividing our data set into training and test sets, and calculating predictions.

ACKNOWLEDGEMENTS

I would like to thank Dr. John R. Ford, Dr. Ryan G. McClarren, Dr. Sunil S. Chirayath, Dr. John C. Keyser, Dr. Karen Vierow, and the Office of Graduate Studies for their support.

NOMENCLATURE

b	Barn
1DWM	One-Dimensional Transport Model with Wall Migration
MCNP	Monte Carlo N-Particle Code
1DW/O	One-Dimensional Transport Model without Wall Migration
GLM	Generalized Linear Model
MLE	Maximum Likelihood Estimation
IRLS	Iteratively Re-weighted Least Squares Regression

TABLE OF CONTENTS

Page

LIST OF FIGURES

LIST OF TABLES

I. INTRODUCTION

Prinja and Pomraning first developed a one-dimensional model, as well as subsequently improved models, for neutral particle transport in ducts as an approximation, using physical arguments to derive a transport equation [1]. Larsen concurrently developed a rigorous mathematical formulation of the same one-dimensional model, and demonstrated its equivalence to the lowest order approximation of a chain of approximations, derived using a method of weighted residuals [2]. The weighted residual method is based on using N basis functions to approximate the azimuthal and transverse components of the particle distribution function in the duct, and N weight functions to transform the original domain to a subspace (z, μ). In each model the stated quantities of interest were reflection and transmission probability.

Under the weighted residual method, Prinja and Pomraning's treatment is equivalent to an $N = 1$ model, with single basis and weight functions. Prinja proceeded to expand the model to account for wall migration for one speed particles, resulting in a nonlocal transport equation, with the scattering kernel displaying spatial memory [3]. For a semi-infinite duct, Prinja solves the transport equation by a Laplace transform Wiener-Hopf technique, and numerical results are provided for the albedo as a function of incident particle direction, probability of absorption in the duct walls, and degree of nonlocal reemission.

Larsen developed an $N = 2$ model by formulating basis and weight functions to treat a semi-infinite duct, with an isotropic particle source distributed uniformly along the wall's inner surface [2]. Using the same parameters as Larsen, Garcia developed the $N = 3$ one-dimensional model, first by deriving a required third basis function, and

subsequently by applying an "analytical discrete ordinates" method [4, 5]. Garcia, moreover, used the one-dimensional duct model, applying both two and three basis function approximations, to solve the problem of energy-dependent neutral particle transport. The matrix transport equation in one spatial dimension, which results from the energy-dependent case, is solved with a numerical version of the discrete ordinates method.

Each subsequent N model demonstrated vastly improved precision. For circular ducts with length to radius ratios between 0.1 and 10, Garcia reported a maximum error of over 300% in the transmission probability for the $N = 1$ model, while for the $N = 2$ and $N = 3$ maximum error values, produced in the reflection probability, are only 9% and 5% [5]. Given that the one-dimensional model is based on a variety of approximations, Garcia tested for the most "severe of approximations" by using multigroup albedos to describe particle reflection in the wall. An unmodified version of MCNP was, as such, used to simulate neutron transport with migration in the walls for ducts of fixed length and wall thickness of 100 cm and 20 cm, and the results were compared to both the $N = 3$ albedo model and modified MCNP simulations with multigroup albedos in the walls [7]. A comparison of the results indicate fairly uniform agreement between the $N = 3$ model and the modified MCNP without wall migration simulations, however there is very poor agreement once accounting for wall migration. For circular concrete ducts, ranging in radius from 8 cm to 50 cm, Garcia reports a maximum error of 170% for reflection probability, while for iron ducts of the same dimensions, he reports a maximum error of approximately 116%. The transmission probabilities in identical concrete and iron systems give maximum errors of approximately 22% and 28% [6].

The results reported by Garcia indicated a need for development of a one-dimensional

model, for two and three basis functions, which can properly account for wall migration. When a particle strikes the wall and is reflected, the albedo model merely supposes that it will reappear at the point of incidence; this is an inadequate approximation given that particles actively migrate in the walls. Garcia reports that in the albedo model up to 50% of the particles reflected by the wall, just at the duct's edge, will leave the system through the duct entrance without a second interaction [6]. The early exit of particles in the albedo model leads to a vast overestimation of the reflection probability, and underestimation of the transmission probability . Moreover, the overestimation of the reflection probability can be expected to increase proportionally to the mean free path of particles in the walls, and inversely proportionally to the duct radius for a fixed length. In this work we treat the problem of neutral particle transport in a duct with wall migration by incorporating the kernel density proposed by Prinja into the third order approximation of the one-dimensional model, and solving it numerically using a matrix form of discrete ordinates.

Neutral particle transport in ducts with wall migration is intrinsically a three-dimensional problem, which has been historically approached by Monte Carlo and view factor methods. However, these methods are computationally taxing, and depending on the duct's shielding material and the number of histories, codes can take on the order of minutes to hours to reach completion. Moreover, Monte Carlo codes such as MCNP have distribution restrictions, and may be inaccessible to segments of the nuclear research community. As such, we develop logistic regression models using the R language for statistical computing [8], which provide analytical expressions, and can be instantly solved without the need for codes (or a computer).

The logistic regression models are dependent on three explanatory variables— duct radius (r), length (L), and shielding thickness (S). Each of the independent parame-

ters are explored via univariate models, where the remaining variables are held fixed. The results of the univariate models reveal that the behavior of neutral particles within the duct and walls can be captured by composite expressions consisting of linear, exponential, and logarithmic functions. Both the one-dimensional model and the logistic regression models are tested for three shielding materials (iron, graphite, and concrete), for both a thermal and 14 MeV neutron source. The analytical expressions of the logistic regression model are evaluated by randomly dividing our data set into training and test sets—i.e. unseen data—and calculating predictions.

II. APPROXIMATE ONE-DIMENSIONAL MODELS FOR NEUTRAL PARTICLE TRANSPORT IN DUCTS

Prinja and Pomraning first developed an approximate one-dimensional model predicated upon on averaging particle-wall collision distances over the duct's surface and the azimuthal angle [1]. The duct is assumed to be evacuated, and subject to a monoenergetic neutral particle source. Particles are introduced into the duct through an open end and stream until striking the inner duct walls. Upon wall collision, the particles are either scattered into the interior of the duct, according to a probability c, or absorbed, according to a probability $1 - c$. As such, particles are strictly removed from the system by wall absorption or by streaming out of the duct ends.

In the one-dimensional model, a duct is considered parallel to the z-axis, with position coordinates (x, y, z). The duct has a length $0 \leq z \leq Z$, and a cross-section (assumed convex) which can be described— independent of z— by the function $h(x, y)$ [1],

$$R : h(x, y) < 0, \tag{1a}$$

$$\partial R : h(x, y) = 0, \tag{1b}$$

where R defines the duct interior, and ∂R defines the duct's interior wall. For example, a circular duct with radius ρ can be described by

$$R : \rho^2 - x^2 + y^2 < 0, \tag{2a}$$

$$\partial R : \rho^2 - x^2 + y^2 = 0. \tag{2b}$$

The boundary conditions at the ends of a duct of length Z are the prescribed incident fluxes

$$\Psi(x, y, 0, \vec{\Omega}) = f(\mu) \quad , h < 0, \mu > 0, \tag{3a}$$

$$\Psi(x, y, Z, \vec{\Omega}) = g(\mu) \quad , h < 0, \mu < 0, \tag{3b}$$

where $f(\mu)$ and $g(\mu)$ are well defined functions. The cross-sectional area and duct perimeter are expressed as

$$A = \int_R dxdy, \tag{4a}$$

$$L = \int_{\partial R} ds, \tag{4b}$$

where ds is the arc length element. Particles in the duct stream with direction $\vec{\Omega}$, which is defined in terms of μ (i.e. the polar angle with respect to the z-axis) as well as a corresponding azimuthal angle ϕ. The direction vector is defined as

$$\begin{aligned} \vec{\Omega} &= (\sin\theta\cos\phi, \sin\theta\sin\phi, \sin\theta\cos\phi) \\ &= (\sqrt{1-\mu^2}\cos\phi, \sqrt{1-\mu^2}\sin\phi, \mu), \end{aligned} \tag{5}$$

and $\vec{\Omega}$ can now be rewritten as

$$\vec{\Omega} = \sqrt{1-\mu^2}\vec{\omega} + \mu\vec{e}, \tag{6}$$

where $\vec{e} = (0, 0, 1)$, and $\vec{\omega} = (\sin\phi, \cos\phi, 0)$. For particles emitted into the interior of the pipe, the range of μ is $-1 \leq \mu \leq 1$, while ϕ ranges from $0 \leq \phi \leq \pi$. The range of the azimuthal angle corresponds to inward directions relative to the walls

of the duct; where $\phi = \frac{\pi}{2}$ refers to a particle emitted parallel to the local inward normal to the wall. The local inward normal can be taken to be a y-axis, where ϕ is measured with respect to a local x-axis. Fig. 1 provides a detailed illustration of the duct geometry.

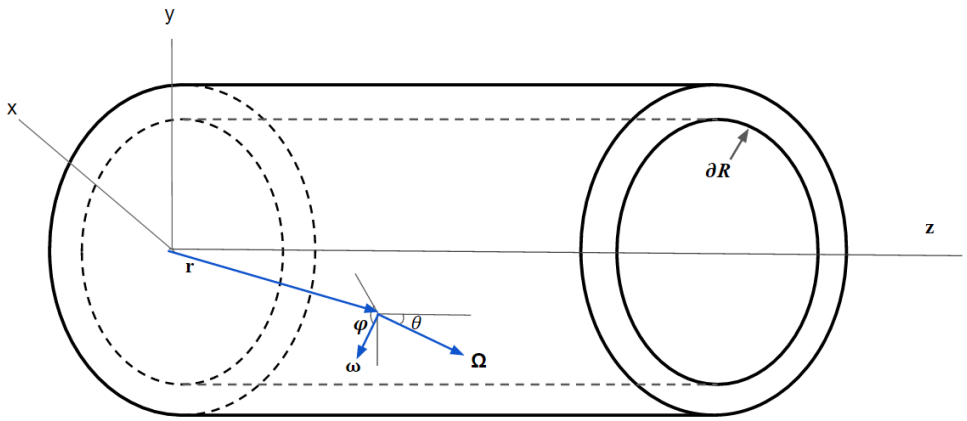

Fig. 1: Duct geometry. [4]

II.A. A Heuristic Approach

A one-dimensional transport equation can be derived based on geometric arguments, as done by Prinja and Pomraning. What follows is a summary of their heuristic approach, according to the description of the duct system introduced in the previous section.

A neutral particle is considered at the origin with coordinates (x_0, y_0, z_0). For a line equation passing through $\vec{r}_0 = (x_0, y_0, z_0)$, and coinciding with the direction $\vec{\Omega}$, a

vector $\vec{r} = \vec{r_0} + \vec{\Omega} t$, can be defined such that,

$$< x, y, z > = < x_0, y_0, z_0 > + \, t \, \vec{\Omega}, \tag{7}$$

$$< x, y, z > = < x_0, y_0, z_0 > + \, t \, (\sqrt{1-\mu^2}\cos\phi, \sqrt{1-\mu^2}\sin\phi, \mu), \tag{8}$$

where solving for t gives us the following equalities:

$$\frac{x - x_0}{\sqrt{1-\mu^2}\cos\phi} = \frac{y - y_0}{\sqrt{1-\mu^2}\sin\phi} = \frac{z - z_0}{\mu}. \tag{9}$$

A streaming distance, λ, for the emitted particle can be defined as

$$\lambda^2 = (x - x_0)^2 + (y - y_0)^2 + (z - z_0)^2. \tag{10}$$

Now combining Eqs. (9-10) gives the following

$$\lambda^2 = \frac{(\sqrt{1-\mu^2}\cos\phi)^2 + \mu^2}{(\sqrt{1-\mu^2}\sin\phi)^2}(y - y_0)^2 + (y - y_0)^2,$$

$$= \frac{(\sqrt{1-\mu^2}\cos\phi)^2 + (\sqrt{1-\mu^2}\sin\phi)^2 + \mu^2}{(\sqrt{1-\mu^2}\sin\phi)^2}(y - y_0)^2,$$

where an expression for λ can now be written as

$$\lambda = \frac{|y - y_0|}{\sqrt{1-\mu^2}\sin\phi}. \tag{11}$$

Eq. (11) indicates the distance traveled by particles, regardless of the duct geometry, has a μ dependence, i.e. $(1-\mu^2)^{-\frac{1}{2}}$. In order to remove any dependence on the particle's azimuthal angle or position, λ is averaged over ϕ and the surface of the duct:

$$\hat{\lambda}(\mu) = \frac{\int_S \vec{ds} \int_0^\pi d\phi(\vec{n}\cdot\vec{\Omega})\lambda}{\int_S \vec{ds} \int_0^\pi d\phi(\vec{n}\cdot\vec{\Omega})}, \tag{12}$$

where $\vec{n}\cdot\vec{\Omega} = (1-\mu^2)^{\frac{1}{2}}\ \sin\phi$, and this factor accounts for the number of particles emitted from an isotropic distribution in the direction $\vec{\Omega}$. If S defines the perimeter of the duct, Eqs. (9-11) imply

$$\hat{\lambda}(\mu) = \frac{1}{2S(1-\mu^2)^{\frac{1}{2}}} \int_S \vec{ds} \int_0^\pi\ |y-y_0|\ d\phi. \tag{13}$$

The double integral can be algebraically eliminated, and λ is reduced to a simple expression,

$$\hat{\lambda} = \frac{\pi V}{S(1-\mu^2)^{\frac{1}{2}}}, \tag{14}$$

where V is defined as the volume per unit length (i.e. the cross sectional area of the pipe). If the cross section is defined as $\Sigma = \frac{1}{\hat{\lambda}(\mu)}$, and dimensionless primed variables are introduced,

$$z' = \frac{Sz}{\pi V}; \quad Z' = \frac{SZ}{\pi V}, \tag{15}$$

as well as a corresponding particle distribution function,

$$\Psi'(z',\mu) = \Psi(z,\mu), \tag{16}$$

then the transport equation can be expressed as [1]

$$\mu\frac{\partial\Psi(z,\mu)}{\partial z} + (1-\mu^2)^{\frac{1}{2}}\Psi(z,\mu) = c\int_{-1}^{1}(1-\mu'^2)^{\frac{1}{2}}\ \Psi(z,\mu')\ d\mu'\ p(\mu'\rightarrow\mu), \tag{17}$$

and the boundary conditions are expressed as

$$\Psi(0,\mu) = f(\mu),\ \mu > 0, \tag{18a}$$

$$\Psi(Z,\mu) = g(\mu),\ \mu < 0, \tag{18b}$$

where the primes have been dropped from each of the pertinent variables for Eqs. (16-18).

II.B. The "N-group" One-Dimensional Model

While the one-dimensional model developed by Prinja and Pomraning was based on geometric considerations, Larsen demonstrated that the same model could be derived by projecting a five-variable transport equation onto a (z,μ) subspace. Larsen further demonstrated that the Prinja and Pomraning model [1] was equivalent to the lowest order approximation of a hierarchy derived by a method of weighted residuals. What follows is a derivation of the one-dimension model for N-basis functions, largely using Larsen's notation [2].

The general form of the seven-dimensional transport equation is expressed as

$$\frac{1}{v}\frac{\partial\psi}{\partial t} + \vec{\Omega}\cdot\nabla\psi + \Sigma_t\psi = \int_0^\infty \int_{4\pi} \Sigma_s(\vec{\Omega}' \to \vec{\Omega}, E' \to E)\psi \; d\vec{\Omega}' d\vec{E}' + Q, \tag{19}$$

with spatial dimensions $\vec{r}(x, y, z)$, angular dimensions $\vec{\Omega}(\theta, \phi)$, energy E, time t, and the gradient operation, in cartesian coordinates, is $\nabla = (\frac{\partial}{\partial x}, \frac{\partial}{\partial y}, \frac{\partial}{\partial z})$. A constrained expression of the transport equation is applied in the duct system:

$$\vec{\Omega}\cdot\nabla\psi(\vec{r}, \vec{\Omega}) = 0, \tag{20}$$

reducing it to five-variable dependence. The constrained expression assumes a steady-state (no time dependence), monoenergetic system without collisions between particles in an evacuated duct, and no external source. The duct geometry is once more defined according the descriptions in the previous section; i.e in terms of $h(x, y), R, \partial R, A$, and L. The boundary conditions at the ends of a duct of length Z are once more defined as the prescribed incident fluxes,

$$\Psi(x, y, 0, \vec{\Omega}) = f(x, y, \vec{\Omega}) \quad , h < 0, \mu > 0, \tag{21a}$$

$$\Psi(x, y, Z, \vec{\Omega}) = g(x, y, \vec{\Omega}) \quad , h < 0, \mu < 0. \tag{21b}$$

The boundary conditions which describe partial isotropic reflection on the inner wall of the duct are expressed as

$$-\vec{\Omega}\cdot\vec{n} \;\; \Psi(\vec{r}, \vec{\Omega}) = \int_{\vec{\Omega}'\cdot\vec{n} \,>\, 0} p(\vec{r}, \vec{\Omega}' \to \vec{\Omega})\Psi(\vec{r}, \vec{\Omega})\partial\vec{\Omega}'$$

$$h = 0, \;\; \vec{\Omega}\cdot\vec{n} < 0, \tag{22}$$

$$p(x, \vec{\Omega}' \to \vec{\Omega}) = \frac{-c}{\pi}(\vec{\Omega}\cdot\vec{n})(\vec{\Omega}'\cdot\vec{n}), \tag{23}$$

where $\vec{n}$ is the unit outward normal at $\vec{r}$, and integration of Eq. (22) over $\vec{\Omega} \cdot \vec{n}$ confirms c as the probability of wall reflection. Moreover, Eq. (22) tells us that for particles incident upon the walls, with incoming directions $\vec{\Omega}'$, the angle of reflection $\vec{\Omega}$ will point towards the interior If the angular vector is written as expressed in Eq. (6), and boundary conditions are applied, the transport equation can be reformulated as [2]

$$\mu \frac{\partial \Psi}{\partial z} + (1 - \mu^2)^{\frac{1}{2}} \vec{\omega} \cdot \nabla \Psi = 0. \tag{24}$$

The 3-D duct problem is reduced to a 1-D problem using the Galerkin scheme for the method of weighted residuals, where Ψ is approximated as ψ,

$$\psi(x, y, z, \mu, \phi) = \sum_{j=1}^{N} \alpha_j(x, y, \phi) \psi_j(z, \mu), \tag{25}$$

α_j are basis functions, and ψ_j are expansion functions. Using Eq. (25) as an approximation for Ψ yields error terms. As such, the method of weighted residuals requires the error terms to be orthogonal to particular weight functions $\beta_i(x, y, \phi)$, for $1 \leq i \leq N$, leading to a number of moment equations. The moment equations are obtained from the stated boundary conditions and the transport equations as expressed in Eq. (24): [2]

$$\int_R \int_0^{2\pi} \beta_i \left[\mu \frac{\partial \psi}{\partial z} + (1 - \mu^2)^{\frac{1}{2}} \vec{\omega} \cdot \nabla \psi \right] = 0, \tag{26}$$

$$\int_{\partial R}\int_{\vec{\omega}\cdot\vec{n}<0}\beta_i\left[\vec{\Omega}\cdot\vec{n}\psi-\frac{c}{\pi}\int_{\vec{\Omega}\cdot\vec{n}>0}(\vec{\Omega}\cdot\vec{n})(\vec{\Omega'}\cdot\vec{n})\times\psi(\vec{\Omega'})d\vec{\Omega'}\right]d\phi ds=0, \tag{27}$$

$$\int_R\int_0^{2\pi}\beta_i\left[\Psi(x,y,0,\vec{\Omega})-f(x,y,\vec{\Omega})\right]=0,\mu>0, \tag{28}$$

$$\int_R\int_0^{2\pi}\beta_i\left[\Psi(x,y,Z,\vec{\Omega})-g(x,y,\vec{\Omega})\right]=0,\mu<0. \tag{29}$$

The basis and weight functions are assumed to satisfy orthogonality:

$$\frac{1}{2\pi A}\int_R\int_0^{2\pi}\beta_i\ \alpha_j\ \partial\phi\partial x\partial y=\delta_{ij},\quad 1\leq i,\quad j\leq N, \tag{30}$$

where the Kronecker delta function is expressed as,

$$\delta_{ij}=\begin{cases}0 & \text{if } i\neq j\\ 1 & \text{if } i=j\end{cases}. \tag{31}$$

Imposing the condition of orthogonality to prescribed basis α_j and weight β_i functions as stated in Eq. (30), coupled with the moment equations, clearly implies

$$\psi_i=\frac{1}{2\pi}\int_R\int_0^{2\pi}\beta_i\psi\ \partial\phi\partial x\partial y, \tag{32}$$

That is, each expansion function can be expressed as the product of a corresponding weight function and the approximation ψ, integrated over the volume of the duct. Ultimately, meeting the conditions stated in Eqs. (26-32) leads to a coupled set of

N transport equations (and corresponding boundary conditions) for the coefficients of the approximation $\psi_j(z,\mu),\ j=1,2,...,N$, as is shown in the proceeding steps.

By application of the vector identity

$$\beta_i\vec{\omega}\cdot\vec{\nabla}\psi=\vec{\omega}\cdot\vec{\nabla}(\beta_i\psi)-\psi\vec{\omega}\cdot\vec{\nabla}\beta_i. \tag{33}$$

Eq. (26) can be expressed as [9]

$$\int_R\int_0^{2\pi}\beta_i\left[\mu\frac{\partial\psi}{\partial z}+(1-\mu^2)^{\frac{1}{2}}\cdot(\vec{\omega}\cdot\nabla(\beta_i\psi)-\psi\vec{\omega}\cdot\nabla\beta_i)\right]\,d\phi dxdy=0, \tag{34}$$

and, applying the divergence theorem, an arc length integral can be introduced as follows

$$\int_R\int_0^{2\pi}\vec{\omega}\cdot\nabla(\beta_i\psi)\,d\phi dxdy=\int_{\partial R}\int_0^{2\pi}\vec{\omega}\cdot\vec{n}\,\beta_i\psi\,d\phi ds. \tag{35}$$

If ψ is now expressed in its approximate form and Eq. (32) is applied, Eq. (34) is written as

$$\mu\frac{\partial\psi_i}{\partial z}=\frac{-(1-\mu^2)^{\frac{1}{2}}}{2\pi A}\times\left(\int_{\partial R}\int_0^{2\pi}\vec{\omega}\cdot\vec{n}\beta_i\,\psi d\phi ds-\int_R\int_0^{2\pi}\psi\nabla\vec{\beta_i}\,d\phi dxdy\right). \tag{36}$$

The arc length integral term in the preceding equation can be broken up as a sum over cases $\vec{\omega}\cdot\vec{n}>0$ and $\vec{\omega}\cdot\vec{n}<0$, where substituting Eq. (27) into the latter case

gives [2]

$$k\mu\frac{\partial\psi_i}{\partial z} = \int_{\partial R}\int_{\vec{\omega}\cdot\vec{n}>0} \vec{\omega}\cdot\vec{n}\beta_i\psi d\phi ds + \int_{\partial R}\int_{\vec{\omega}\cdot\vec{n}<0} \vec{\omega}\cdot\vec{n}\beta_i \\ \times\left[\frac{c}{\pi}\int_{\vec{\Omega}\cdot\vec{n}>0}\vec{\Omega'}\cdot\vec{n}\psi(\vec{\Omega'})d\vec{\Omega'}\right]d\phi ds - \int_{\partial R}\int_0^{2\pi}\psi\vec{\omega}\cdot\nabla\beta_i d\phi dxdy, \quad (37)$$

and $k = \frac{-2\pi A}{(1-\mu^2)^{\frac{1}{2}}}$. If the integrals over $\vec{\Omega'}\cdot\vec{n}$ are written according to the identity

$$\int_{\vec{\Omega'}\cdot\vec{n}}(\vec{\Omega'}\cdot\vec{n})(\cdot)d\vec{\Omega} = \int_{\vec{\omega}\cdot\vec{n}>0}\vec{\omega'}\cdot\vec{n}\int_{-1}^{1}d\mu'(1-\mu^2)^{\frac{1}{2}}(\cdot)d\phi', \quad (38)$$

and Eq. (26) is applied to Eq. (37), the general matrix form of the transport equation with N basis functions,can now be written as [2]

$$\mu\frac{\partial\Psi(z,\mu)}{\partial z} + (1-\mu^2)^{\frac{1}{2}}\mathbf{A}\ \Psi(z,\mu) \\ = \frac{2c}{\pi}(1-\mu^2)^{\frac{1}{2}}\ \mathbf{B}\ \int_{-1}^{1}(1-\mu'^2)^{\frac{1}{2}}\ \Psi(z,\mu')\partial\mu'. \quad (39)$$

The boundary conditions are given as column vectors,

$$\Psi(0,\mu) = \mathbf{F}(\mu); \Psi(Z,-\mu) = \mathbf{G}(\mu), \quad (40)$$

where the components ψ_i are expressed as

$$\psi_i(0,\mu) = \frac{1}{2\pi A}\int_R\int_0^{2\pi}\beta_i f\ d\phi dxdy,\ \mu>0, \quad (41)$$

$$\psi_i(Z,\mu) = \frac{1}{2\pi A}\int_R\int_0^{2\pi}\beta_i g\ d\phi dxdy,\ \mu<0. \quad (42)$$

A and **B** are $N \times N$ matrices consisting of elements a_{ij}, b_{ij}, which follow directly from the derivation of Eq. (39)

$$a_{ij} = \frac{1}{2\pi A}[\ \int_{\partial R}\int_{\omega\cdot n>0} \vec{\omega}\cdot\vec{n}\ \beta_i\alpha_j d\phi ds - \int_R\int_0^{2\pi} (\vec{\omega}\cdot\nabla\beta_i)\ \alpha_j d\phi ds\ ], \tag{43}$$

$$b_{ij} = \frac{1}{4\pi A}\int_{\partial R}\left(\int_{\omega\cdot n<0}\vec{\omega}\cdot\vec{n}\right)\beta_i d\phi\ \times\left(\int_{\vec{\omega}\cdot\vec{n}>0}\vec{\omega}\cdot\vec{n}\ \alpha_j d\phi\right)ds. \tag{44}$$

The matrix form of the transport equation with N basis functions and corresponding boundary conditions, applied to a duct of arbitrary cross-sectional geometry, constitute the general model. Therefore, in order to make use of the model, the duct geometry, α_i, and β_i must be specified and the matrix components a_{ij} and b_{ij} must evaluated.

It should be noted that the one-dimensional model introduces angular dependence into the cross-sections, leading to the following interpretation: in a duct of infinite length, a particle starting at position $\vec{r}$ will travel a deterministic distance [2],

$$l = (1-\mu^2)^{\frac{-1}{2}}\ D(x,y,-\vec{\omega}), \tag{45}$$

before striking a duct wall. The function $D(x,y,-\vec{\omega})$ is defined as the distance from an arbitrary point (x,y,z) in the duct interior to the inner wall ∂R along the direction $-\vec{\omega}$. As such, particles in the duct travel a distance proportional to $(1-\mu^2)^{\frac{-1}{2}}$ before colliding with an inner wall; this distance was interpreted by Prinja and Pomraning as a mean-free-path [1], implying that the cross-section is proportional to $(1-\mu^2)^{\frac{1}{2}}$.

II.C. Basis Functions

The basis functions for the $N = 3$ model are derived independently by Larsen and Garcia. In each case, a Galerkin scheme was used to select the corresponding weight functions, i.e. $\beta_i(x, y, \phi) = \alpha_i(x, y, \phi)$ for $i = 1, 2, 3$. The first and second basis functions are expressed as [2, 4]

$$\alpha_1(x, y, \phi) = 1, \tag{46}$$

$$\alpha_2(x, y, \phi) = u[D(x, y, \vec{\omega}) - v], \tag{47}$$

where u and v are constants. The first two basis functions are linear combinations of 1 and D, where this choice is justified by the following arguments. For an arbitrary point $\vec{r}$ on the inner duct wall, $S(\vec{r}_0)$ is defined as the distribution of particles scattered into the duct. Now, for a point $\vec{r}$ in the duct's interior and an angle $\vec{\Omega}$, where

$$\vec{r}_0 = \vec{r} - (1 - \mu^2)^{\frac{-1}{2}} \; D(x, y, \vec{\omega}) \; \vec{\Omega}, \tag{48}$$

lies on the duct's inner wall, there exists a corresponding distribution function such that,

$$\psi(\vec{r}, \vec{\Omega}) = S[\vec{r} - (1 - \mu^2)^{\frac{-1}{2}} \; D(x, y, \vec{\omega}) \; \vec{\Omega}]. \tag{49}$$

Expressing the distribution function in terms of D and S indicates that it is a constant along a characteristic curve in a source-free vacuum. If S is weakly dependent on x and y, then the distribution function can be rewritten as

$$\psi(\vec{r}, \vec{\Omega}) \approx S[z - (1 - \mu^2)^{\frac{-1}{2}} \; D(x, y, \vec{\omega})]. \tag{50}$$

Eq. (50) shows that $\psi(\vec{r},\vec{\Omega})$ only depends on x, y and ϕ via the function D. Moreover, if S is weakly varying with respect to z, the distribution can be written as

$$\psi(\vec{r},\vec{\Omega}) \approx S(z) - (1-\mu^2)^{\frac{-1}{2}}\ D(x,y,\vec{\omega})\ \frac{dS}{dz}, \tag{51}$$

where the derivative is considerably smaller than S; this result indicates that the $\psi(\vec{r},\vec{\Omega})$ is virtually independent of x, y, and ϕ, justifying the choice of basis functions as linear combinations of 1 and D. However, it should be noted that the preceding arguments apply to long ducts, where $S(z)$ is weakly varying and edge effects can be considered negligible.

The constants v and u, upon which the second basis function depends, are given as

$$v = \frac{1}{2\pi}\int_R \int_0^{2\pi} D(x,y,\vec{\omega})\partial\phi\partial x\partial y, \tag{52}$$

$$u = \left(\frac{1}{2\pi}\int_R \int_0^{2\pi} [D(x,y,\vec{\omega}) - v]^2\partial\phi\partial x\partial y\right)^{\frac{-1}{2}}. \tag{53}$$

Given the definition of $D(x,y,\vec{\omega})$, as the distance in the (x,y) plane, from a point in the duct to the inner wall, the following properties can be asserted:

$$\vec{\omega}\cdot\nabla D(x,y,\vec{\omega}) = 1, \quad (x,y)\in R, \tag{54}$$

$$D(x,y,\vec{\omega}) = 0,\ (x,y)\in\partial R, \quad \vec{\omega}\cdot\vec{n} < 0, \tag{55}$$

$$D = (\vec{\omega}\cdot\nabla D^2)/2, \tag{56}$$

$$(D-v)^2 = [\vec{\omega}\cdot\nabla(D-v)^3]/3, \tag{57}$$

which allows for v and u to be expressed in terms of arc length integrals

$$v = \frac{1}{4\pi} \int_R \int_0^{2\pi} (\vec{\omega} \cdot \nabla D^2) d\phi ds, \tag{58}$$

$$u = \left[\frac{1}{6\pi} \int_{\partial R} \int_0^{2\pi} \vec{\omega} \cdot \vec{n} (D - v) \right]. \tag{59}$$

The third basis function is expressed as a linear combination of 1, $D(x, y, \vec{\omega})$, and $D^2(x, y, \vec{\omega})$ based on earlier arguments [4]

$$\alpha_3(x, y, \phi) = r[D(x, y, \vec{\omega}) - s][D(x, y, \vec{\omega}) - t], \tag{60}$$

where r, s, and t are constants. Noting the conditions of orthogonality for i=1 and j=3, as well as for i=2 and j=3, the constants s and t must satisfy

$$(s - v)(t - v) = \frac{-1}{u^2}, \tag{61}$$

$$s + t = 2v + q, \tag{62}$$

where the following algebraic manipulations can be applied in order to find expressions for s and t independent of each other,

$$t = 2v + q - s,$$

$$\Rightarrow (s - v)(v + q - s) = \tfrac{-1}{u^2},$$

$$\Rightarrow s^2 - s(2v - q) + (v^2 + vq - u^{-2}) = 0,$$

which implies,

$$s = v + \frac{1}{2}(q + \sqrt{q^2 + 4/u^2}). \tag{63}$$

Proceeding with same steps used to find s, t can be expressed as

$$t = v + \frac{1}{2}(q - \sqrt{q^2 + 4/u^2}), \tag{64}$$

where the constant q is defined as

$$q = \frac{u^2}{2\pi} \int_R \int_0^{2\pi} [D(x, y, \vec{\omega}) - v]^3 d\phi dx dy. \tag{65}$$

Substituting the definitions of s and t into the third basis function gives,

$$\alpha_3(x, y, \phi) = r[D(x, y, \vec{\omega} - v)][D(x, y, \omega) - v - q] - \frac{r}{u^2}, \tag{66}$$

where the orthogonality condition, expressed by Eq. (30), leads to definition of r as

$$r = \left[\frac{1}{2\pi} \int_R \int_0^{2\pi} [D(x, y, \vec{\omega}) - v]^4 \partial\phi \partial x \partial y - \frac{(q^2 + \frac{1}{u^2})}{u^2} \right]^{\frac{1}{2}}. \tag{67}$$

As previously noted, the basis and weights functions are not directly expressed in the multi-basis function form of the transport equation. Rather, these functions compose the elements of the matrices **A** and **B**, which are required to apply the model. Having explicit statements of the first thee basis functions, as well as their dependencies (constants: u, v, q, r), exact expressions for the matrix elements can be found by direct substitution into Eqs. (43,44). Below, each of the eighteen elements

for the $N = 3$ model are listed [4]:

$$a_{11} = b_{11} = L/(\pi A) \tag{68a}$$

$$a_{12} = b_{12} = u - uvL/(\pi A) \tag{68b}$$

$$a_{21} = b_{21} = -uvL/(\pi A) \tag{68c}$$

$$a_{22} = u^2 v^2 L/(\pi A) \tag{68d}$$

$$b_{22} = -uv[u - uvL/(\pi A)] \tag{68e}$$

$$a_{13} = b_{13} = -qr + (v^2 + qv - 1/u^2) rL/(\pi A) \tag{68f}$$

$$a_{31} = b_{31} = (v^2 + qv - 1/u^2) rL/(\pi A) \tag{68g}$$

$$a_{23} = (2r/u) - (v^2 + qv - 1/u^2) uvrL/(\pi A) \tag{68h}$$

$$b_{23} = uv[qr - (v^2 + qv - 1/u^2) rL/(\pi A)]. \tag{68i}$$

$$a_{32} = -(v^2 + qv - 1/u^2) uvrL/(\pi A) \tag{68j}$$

$$b_{32} = r(v^2 + qv - 1/u^2)[u - uvL/(\pi A)] \tag{68k}$$

$$a_{33} = (v^2 + qv - 1/u^2)^2 r^2 L/(\pi A) \tag{68l}$$

$$b_{33} = -r(v^2 + qv - 1/u^2)[qr - (v^2 + qv - 1/u^2) rL/(\pi A)]. \tag{68m}$$

Based on the stated results, the $N = 3$ model depends entirely on six parameters: $A, L, u, v, q,$ and r (and four for the $N = 2$ model, where q and r are excluded). These parameters must account for the duct geometry and orthogonality conditions.

II.D. Wall Migration Model: Methods and Parameters

In this work, we develop a nonlocal transport equation that accounts for particle migration into duct walls, composed of a specified material, using the $N = 3$ one-dimensional model. This equation will be specifically applied to ducts with iron,

concrete, and graphite walls, subject to a thermal neutron source.

The N-basis functions model developed by Larsen was applied strictly to the case where duct walls either reflect or absorb particles, without accounting for wall migration or wall (shielding) material. Garcia subsequently applied an albedo approximation in order to account for wall materials, for a multi-group case [6], but also excluded wall migration. In order to account for neutral particles that migrate a fixed distance in the walls and undergo diffuse emission, Prinja introduced a nonlocal kernel density $K(z \to z')$, strictly for the $N = 1$ case (i.e. the original, heuristic model), without accounting for wall materials [3]. The kernel density satisfies the condition

$$\int_{-\infty}^{\infty} K(z' \to z) = 1, \tag{69}$$

where this ensures that the particle is re-emitted within the duct. In order to realize an exact solution, Prinja proposed an exponential function (consistent with particle attenuation within wall material) expressed as [3]

$$K(z' \to z) = \frac{\lambda}{2} \exp(-\lambda |z - z'|), \tag{70}$$

where λ is a free parameter. Re-emission profiles are obtained by adjusting λ (large: near-local, small: nonlocal), where

$$\lim_{\lambda \to \infty} K(z' \to z) = \delta(z - z'), \tag{71}$$

ensures recovery of the local model. A full account of wall migration requires inte-

grating the kernel density over the entire length of the duct, where

$$\int_0^Z K(|z-z'|)dz' = \int_0^Z \frac{\lambda}{2} exp(\lambda|z-z'|), \tag{72}$$

is introduced into the transport equation. Accounting for wall migration via the kernel density, the 1-D duct model transport equation can now be expressed as

$$\mu\frac{\partial\Psi(z,\mu)}{\partial z} + (1-\mu^2)^{\frac{1}{2}}\mathbf{A}\ \Psi(z,\mu) = \frac{2c}{\pi}(1-\mu^2)^{\frac{1}{2}} \times \mathbf{B}\ \int_0^Z \partial z' \int_{-1}^1 (1-\mu'^2)^{\frac{1}{2}}\ K(z'\rightarrow z)\ \Psi(z,\mu')\partial\mu', \tag{73}$$

where Z is the length of the duct. From Eq. (73) it is clear that in addition to the basis and weight functions, the parameters λ and c must be defined in order to apply the model accounting for wall migration. The free-parameter λ is expressed as the mean distance that incident particles travel in the walls before re-emerging (in cm),

$$\lambda = \frac{1}{d}. \tag{74}$$

The parameter c defines the wall reflection probability. However, λ and c cannot be directly calculated; treating the walls as a plane layer, these parameters are approximated using MCNP simulations for an equivalent disk problem [6] subject to a thermal neutron source. Comparable to the equivalence proposed by Garcia [6], simulations are performed for a point source located the center of a planar surface corresponding to a 20 cm-thick disk with a 100 cm radius. The wall migration parameters are calculated for each of three materials: iron, concrete, and graphite. Table I provides a summary of the values of c—calculated as the current ratio— for each of the wall materials.

Table I: Values for wall reflection probability computed using MCNP for 10^6 histories.

Material	c
Iron	0.54
Concrete	0.70
Graphite	0.85

Using MCNP's PTRAC function, which follows the life of individual particles including terminal events, the mean distance that particles travel in the disk can be calculated. PTRAC returns a convoluted output with millions of data points, and a parsing code is used to calculate the distance traveled by each particle as well as the mean (this process will be discussed in further detail in a later section). Table II provides a summary of the PTRAC results.

Table II: Mean distance d (cm) traveled in walls computed using MCNP for 10^6 histories, and material density ρ (g/cm^3).

Materials	d	ρ
Iron	1.065	7.87
Concrete	2.80	2.30
Graphite	5.905	1.70

It should be noted that the distance traveled by the particles in each case is inversely proportional to the density of the wall material. Moreover, the distance values are

consistent with the absorption cross-sections for thermal neutrons for each of the materials—where iron has a cross-section (E-2 b) one magnitude larger than the graphite and concrete (E-3 b). Fig. 2 shows the distribution of distances traveled in the duct walls by particles, for each of the specified materials.

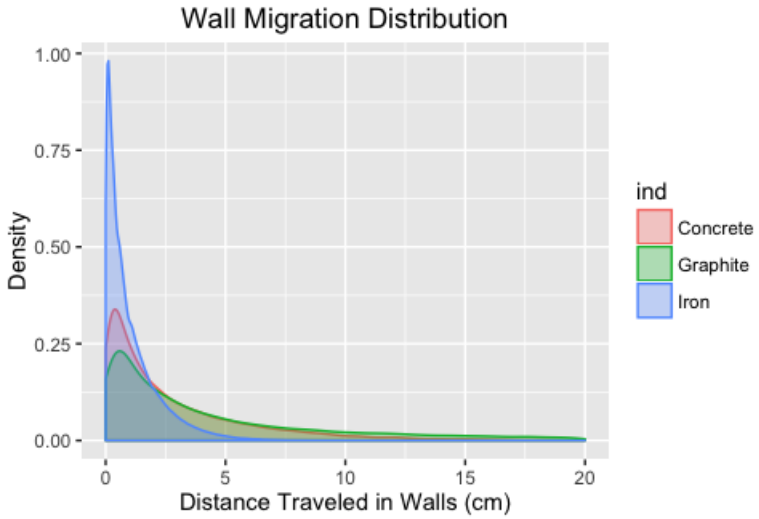

Fig. 2: Distances traveled by particles in the disk.

Accounting for the wall reflection constant and the kernel density, as well the matrix elements of $\mathbf{A}$ and $\mathbf{B}$, the $N = 3$ nonlocal transport equation can be fully solved using numerical methods.

III. DISCRETE ORDINATES SOLUTION TO $N = 3$ MODEL

III.A. The Discrete Ordinates Approximation

The discrete ordinates method allows for the integro-differential transport equation to be solved numerically by evaluating the angular distribution of particle flux at a specified number of discrete directions (that is, applying a discrete treatment of the angular variable $\vec{\Omega}$), coupled with spatial discretization ("zones"). In theory, by increasing the number of angles and zones under consideration the accuracy of solutions can be improved; as such, the accuracy is merely limited by computational resources [10]. Of particular importance in the application of the discrete ordinates method is the choice of angles, and the approximation of the integrals over the direction variable. These issues will be considered in the context of the planar, isotropic scattering, monoenergetic, steady-state form of the integro-differential transport equation without external sources (which has the same form as the nonlocal transport equation) [10]:

$$\mu \frac{\partial \Psi(z,\mu)}{\partial z} + \Sigma_t(z)\Psi(z,\mu) = \frac{c(z)\Sigma_s(z)}{2} \int_{-1}^{1} \Psi(z,\mu')\partial\mu', \tag{75}$$

where Σ_t is the total cross-section, and Σ_s is the scattering cross-section. Considering a set of discrete directions $\mu_n = \mu_1, \mu_2, ..., \mu_N$ and a set of corresponding weights $w_n = w_1, w_2, ..., w_N$, the scattering integral in Eq. (75) is approximated by Gaussian quadrature for μ dependent Ψ:

$$\int_b^a \Psi(\mu')\partial\mu' \approx \frac{b-a}{2}\sum_{j=1}^{N} w_j \Psi\left(\frac{b-a}{2}\mu'_j + \frac{a+b}{2}\right), \tag{76}$$

where N is the number of discrete angles. Converting the domain from [a,b] to [-1,1] —thereby standardizing the weights— the approximation is expressed as

$$\int_{-1}^{1} \Psi(\mu')\partial\mu' \approx \sum_{j=1}^{N} w_j \Psi(\mu'_j). \tag{77}$$

By substituting the quadrature approximation into the planar transport equation, Eq. (76) can be rewritten in discretized form as

$$\mu_n \frac{\partial\Psi(z,\mu_n)}{\partial z} + \Sigma_t(z)\Psi(z,\mu_n) = \frac{c(z)\Sigma_s(z)}{2}\sum_{j=1}^{N} w_j \Psi(z,\mu_j), \tag{78}$$

for $n = 0, 1, ..., N$. Eq. (78) has a similar form to the steady-state, monoenergetic one-dimensional transport equation and represents a set of N coupled differential equations, which can be solved by iteration techniques given the corresponding boundary conditions and specific constraints of the system. In general the directions and quadrature weights are chosen with the objective of optimizing the solution. However, for a slab geometry, three specific constraints must also be considered: [10]

1. Because the integral in the scattering term is always positive, the quadrature weights must also be positive for all cases of n

$$w_n > 0, \text{ for all } n = 1, 2, ..., N$$

2. The choice of directions and quadrature weights must be symmetric about $\mu = 0$ (equal weights coupled with a symmetric angular distribution), for an even number of discrete angles. That is,

$$\mu_n - \mu_{N+1-n}, w_n = w_{N+1-n}, \text{ for } n = 1, 2, ..., \tfrac{N}{2}.$$

Symmetry ensures that equal importance is assigned to particles streaming along each flight direction. Moreover, an even number of directions avoids choosing a value of n that results in $\mu_n = 0$. By necessity, μ cannot be 0, as such a result would lead to the disappearance of the position derivative in Eq. (78):

$$\mu_n = 0 \Rightarrow \mu_n \tfrac{\partial \Psi(x,\mu_n)}{\partial z} = 0.$$

A value of $\mu_n = 0$ would,furthermore, lead the appearance of discontinuities in flux along the angular coordinate.

3. For low orders of μ, and N distinct quadrature points, given $\Psi(x, \mu)$ is a polynomial of degree $N-1, N$ number of weights can be found such that the quadrature formula provides an exact value for the scattering term integral. That is [11],

$$\sum_{n=1}^{N} w_n \mu_n^m = \int_{-1}^{1} \mu^m \partial\mu = \begin{cases} \frac{2}{n+1} & \text{if } (n \text{ even}) \\ 0 & \text{if } (n \text{ odd}) \end{cases}, \tag{79}$$

where $m = 0, 1, 2..., N-1$. Integrals can be solved exactly as $N \to \infty$, however for any finite N, the formula is only exact for linear functions. Given constraints 1-3, it is possible to determine N parameters μ_n and w_n such that polynomials having order $0, 2, ..., 2N-2$ can be exactly integrated. That is,

$$\sum_{n=1}^{N} w_n P_k(\mu_n) P_l(\mu_n) = \int_{-1}^{1} P_k(\mu) P_l(\mu) d\mu = \frac{2\delta_{kl}}{2k+1},$$
$$k, l = 0, 1, ..., N-1, \tag{80}$$

where the Legendre polynomials P_n are generally orthogonal on the interval [-1,1],

and the corresponding weight function w_n is unity [11]. The ordinates are specified as the N roots of the Legendre polynomial of order N,

$$P_N(\mu_i) = 0. \tag{81}$$

The angles μ_n and w_n satisfying the stated conditions constitute the Legendre-Gaussian quadrature set.

A numerical solution is obtained by writing the transport equations in the following form, where Q is defined as the scattering source:

$$\mu_n \frac{\partial \Psi(z,\mu_n)}{\partial z} + \Sigma_t(z)\Psi(z,\mu_n) = Q(z,\mu_n), \tag{82}$$

and solving via an iteration on the source, using a lagging scheme (i.e. source iteration): [10]

$$\mu_n \frac{\partial \Psi^{[s+1]}(z,\mu_n)}{\partial z} + \Sigma_t^{[s+1]}(z)\Psi(z,\mu_n) = Q^{[s]}(z,\mu_n), \tag{83}$$

$$Q^{[s+1]}(z,\mu_n) = \frac{\Sigma_s(2)}{2} \sum_{n=1}^{N} w_n \Psi^{[s+1]}(z,\mu_n). \tag{84}$$

Source iteration is initiated by setting $Q = 0$ and first solving the left side of Eq. (83) using boundary conditions. Having solved for the left side of the equation, Q may be successively updated. In order to implement source iteration, however, spatial discretization must be introduced. That is, for ducts of length a, z:$[0, a]$, the duct is partitioned into I subintervals with uniform properties. Specifically, in each subinterval $z_{i-1} < z < z_i$ the average values of the angular flux, the emission density,

and cross-sections are uniformly defined. Spatial discretization, therefore, allows the planar transport equation to be rewritten as [11]

$$\mu_n \frac{\Psi(z_i, \mu_n) - \Psi(z_{i-1}, \mu_n)}{\Delta z_i} + \Sigma_s \bar{\Psi}_{i,n} = Q_{i,n} \tag{85}$$

where $\Delta z = (z_{i-1}, z_i)$, and $\bar{\Psi}_{i,n}$ is the mesh-averaged angular flux. The algorithm used to solve the discretized transport equation, as expressed in Eq. (85), is described in greater detail in the following section, in the context of the nonlocal one-dimensional form.

III.B. Solution of the Nonlocal One-Dimensional Transport Equation

Accounting for wall migration via the kernel density, the nonlocal one-dimensional transport equation can be compactly expressed as

$$\mu \frac{\partial \Psi(z,\mu)}{\partial z} + (1-\mu^2)^{\frac{1}{2}} \mathbf{A}\ \Psi(z,\mu) = \frac{2c}{\pi}(1-\mu^2)^{\frac{1}{2}} \times \mathbf{B} \int_{-1}^{1} (1-\mu'^2)^{\frac{1}{2}}\ \tilde{\Psi}(z,\mu')\partial\mu'. \tag{86}$$

with boundary conditions

$$\Psi(0, \mu_n) = \mathbf{F}(\mu_\mathbf{n});\ \ \Psi(Z, \mu_n) = \mathbf{G}(-\mu_\mathbf{n}). \tag{87}$$

A Gaussian-Legendre quadrature of order N is used solve the scattering integral term in Eq. (86). In order to perform the numerical integration, the Legendre polynomials

P_n are defined using a recursive rule, such that [12]

$$P_0(\mu) = 1, \tag{88a}$$

$$P_1(\mu) = \mu, \tag{88b}$$

$$n\ P_n(\mu) = (2n-1)\ \mu\ P_{n-1}(\mu) - (n-1)\ P_{n-2}(\mu). \tag{88c}$$

The derivative of P_n can be written as

$$P'_n(\mu) = \frac{n}{\mu^2 - 1}(\mu P_n(\mu') - P_{n-1}(\mu)), \tag{89}$$

and the roots of P_n are approximated using a Newton-Raphson method: [13]

$$\mu_{n+1} = \mu_n - \frac{\Psi(\mu_n)}{\Psi'(\mu_n)}. \tag{90}$$

An initial guess μ_0 for the j-th root of P_n is given as

$$\mu_0 = cos\left(\pi\ \frac{j - 1/4}{n + 1/2}\right). \tag{91}$$

Given the angles μ_j, the weights are calculated by

$$w_j = \frac{2}{(1-\mu_j)^2[P'_n(\mu_j)]^2}. \tag{92}$$

Having calculated both the angles and weights, the scattering term can be integrated according to Eq. (77).

Introducing the quadrature approximation, Eq. (86) is written as

$$\mu_n \frac{\partial \Psi(z,\mu_n)}{\partial z} + (1-\mu_n^2)^{\frac{1}{2}}\ \mathbf{A}\ \Psi(z,\mu_n) = \frac{2c}{\pi}(1-\mu_n^2)^{\frac{1}{2}}\ \mathbf{B}\ \sum_{j=1}^{N}(1-\mu_j'^2)^{\frac{1}{2}}\omega_j \tilde{\Psi}(z,\mu_j), \quad (93)$$

for $n = 1, 2, ..., N$. The flux distribution function $\tilde{\Psi}$ incorporates the kernel density and can be expressed as

$$\tilde{\Psi}(z,\mu_j') = \int_0^Z K(|z-z'|)\ \bar{\Psi}(z',\mu_j')\ dz' = \int_0^Z \frac{\lambda}{2}\exp\left(\lambda|z-z'|\right)\ \bar{\Psi}(z',\mu_j')\ dz', \quad (94)$$

for a duct of length Z. Introducing a spatial mesh z_i, where $i = 0, 1, ..., I$, and integrating over each of the mesh intervals (z_{i-1}, z_i) using a diamond rule approximation,

$$\bar{\Psi}_{i,n} = \frac{1}{2}(\Psi_{i-1,n} + \Psi_{i,n}), \quad (95)$$

the mesh average vectors can be eliminated [4] , and Eq. (94) can be rewritten in the form

$$\frac{\mu_n}{\Delta z}[\Psi_{i,n} - \Psi_{i-1,n}] + (1-\mu_n^2)^{\frac{1}{2}}\ \mathbf{A}\ \frac{1}{2}[\Psi_{i-1,n} + \Psi_{i,n}] = \frac{2c}{\pi}(1-\mu_n^2)^{\frac{1}{2}}\ \mathbf{B}\ \sum_{j=1}^{N}(1-\mu_j'^2)^{\frac{1}{2}}\omega_j\ \frac{1}{2}[\tilde{\Psi}_{i-1,j} + \tilde{\Psi}_{i,j}]. \quad (96)$$

If the right side of Eq. (96) is set equal to $\tilde{Q}_{i,n}$,

$$\frac{\mu_n}{\Delta z}[\Psi_{i,n} - \Psi_{i-1,n}] + (1-\mu_n^2)^{\frac{1}{2}}\ \mathbf{A}\ \frac{1}{2}[\Psi_{i-1,n} + \Psi_{i,n}] = \tilde{Q}_{i,n}, \quad (97)$$

and the boundaries of the mesh intervals are combined as follows

$$\Psi_{i,n}\left(\frac{\mu_n}{\Delta z}+\frac{A(1-\mu^2)^{\frac{1}{2}}}{2}\right)+\Psi_{i-1,n}\left(\frac{\mu_n}{\Delta z}-\frac{A(1-\mu^2)^{\frac{1}{2}}}{2}\right)=\tilde{Q}_{i,n}, \tag{98}$$

$$\Psi_{i,n}M^{+}_{i,n}-M^{-}_{i,n}\Psi_{i-1,n}=\tilde{Q}_{i,n}, \tag{99}$$

equations for $\Psi_{i,n}$ can be written, over values of n, as

$$\Psi_{i,n}=[M^{+}_{i,n}]^{-1}[M^{-}_{i,n}\Psi_{i-1,n}+\tilde{Q}_{i,n}], \quad \mu_n>0, \tag{100a}$$

$$\Psi_{i-1,n}=[M^{-}_{i,n}]^{-1}[M^{+}_{i,n}\Psi_{i,n}+\tilde{Q}_{i,n}], \quad \mu_n<0. \tag{100b}$$

Eqs. (100) are solved using a sweeping technique, initialized by setting the scattering source vector to zero and applying the boundary conditions to Eq. (96), in order to move across the mesh. $M^{\pm}_{k,i}$ have been set to

$$M^{\pm}_{i,n}=\mathbf{I}\frac{|\mu_n|}{\Delta z}\pm\frac{1}{2}(1-\mu_n^2)^{\frac{1}{2}}\mathbf{A}, \tag{101}$$

and $\mathbf{I}$ is the identity matrix. Convergence of the solution is defined when the components of $\Psi_{k,i}$ do not differ by more than 10^{-8} in two successive steps, for $i=0,1,...I$ and $n=1,2,...N$.

III.C. Circular Duct Case

As a test-case, the $N=3$ nonlocal one-dimensional model is applied to a duct of circular cross section with radius ρ. For a circular duct geometry, the function

$D(x, y, \vec{\omega})$ is expressed as [2]

$$D(x, y, \vec{\omega}) = \vec{r} \cdot \vec{\omega} - [(\vec{r} \cdot \vec{\omega})^2 - x^2 - y^2\ ]^{\frac{1}{2}}, \tag{102}$$

and is reduced at the inner wall ∂R to

$$D(x, y, \vec{\omega}) = \begin{cases} 2\rho\ \vec{\omega} \cdot \vec{n} & \text{if } \vec{\omega} \cdot \vec{n} > 0, \\ 0 & \text{if } \vec{\omega} \cdot \vec{n} < 0. \end{cases} \tag{103}$$

The six parameters required to determine the elements of $\mathbf{A}$ and $\mathbf{B}$, and thereby define the $N = 3$ model, are expressed as [4]

$$A = \pi\rho^2, \tag{104}$$

$$L = 2\rho\pi, \tag{105}$$

$$u = 3\pi(9\pi^2 - 64)^{\frac{-1}{2}}\ /\ \rho, \tag{106}$$

$$v = 8\rho\ /\ 3\pi, \tag{107}$$

$$q = 8\rho\left[\frac{9\rho}{5}(9\pi^2 - 64)^{-1} - \frac{2}{3\pi}\right] \tag{108}$$

$$r = \rho^{-2}\left[1 - \frac{576}{25}(9\pi^2 - 64)^{-1}\right]^{\frac{-1}{2}}, \tag{109}$$

where u and v are determined by Eqs. (58-59), q is determined by Eq. (65), and r is determined by Eq. (67).

III.D. Circular Duct Case: Results

The quantities of interest in this case are reflection probability and transmission probability, corresponding to iron, concrete, and graphite ducts, subject to a thermal neutron source. That is, the current ratios at each end of the ducts, are calculated as

$$R = 2\int_0^1 = \mu\Psi_1(0,-\mu)d\mu, \tag{110}$$

$$T = 2\int_0^1 = \mu\Psi_1(Z,\mu)d\mu, \tag{111}$$

for values of c and λ corresponding to each of the wall materials. If the quadrature nodes are ordered such that $-1 > \mu_1 > \cdots > \mu_n > 1$, and $n = N/2$, reflection and transmission probabilities can be expressed in discretized form as [4]

$$R = 2\sum_{j=n+1}^{N} \omega_j|\mu_j|(1-\mu_j^2)^{\frac{1}{2}}\ \Psi(0,\mu_j), \tag{112}$$

$$T = 2\sum_{j=1}^{N} \omega_j\mu_j(1-\mu_j^2)^{\frac{1}{2}}\ \Psi(Z,\mu_j). \tag{113}$$

$\Psi_1(0,\mu_j)$, $j = n{+}1, n{+}2, ...N$, and $\Psi_1(Z,\mu_j)$, $j = 1, 2..., N$, are the discretized results for the first components of the coefficient vectors $\Psi(0,\mu_j)$ for $\mu_j < 0$, and $\Psi(Z,\mu_j)$ for $\mu_j > 0$. The results for Tables III-VIII correspond to a Gaussian quadrature of 640 nodes and weights, coupled with a spatial discretization mesh consisting of 160 intervals.

Reflection and transmission probabilities are calculated for 100 cm ducts with 20 cm thick walls, and compared to MCNP simulations for 10^6 histories. In each table the nonlocal one-dimensional transport model is abbreviated as "1DWM". The percent deviation (% Dev) is calculated as

$$\% \text{ Deviation} = \frac{P_{1DWM} - P_{MCNP}}{P_{MCNP}} \times 100, \tag{114}$$

where P is the reflection or transmission probability.

Table III: Reflection Probability for ducts with iron shielding.

Radius	1DWM	MCNP	% Dev.
8	0.1557	0.1466	6.23
10	0.1597	0.1529	4.48
15	0.1653	0.1621	2.03
20	0.1679	0.1665	0.84
30	0.1691	0.1693	-0.10
50	0.1630	0.1638	-0.49

Table IV: Transmission Probability for ducts with iron shielding.

Radius	1DWM	MCNP	% Dev.
8	0.007950	0.008743	-9.98
10	0.01340	0.014736	-9.95
20	0.03381	0.03716	-9.91
20	0.06262	0.06778	-8.23
30	0.1322	0.1390	-5.12
50	0.2691	0.2751	-2.26

Table V: Reflection Probability for ducts with concrete shielding.

Radius	1DWM	MCNP	% Dev.
8	0.2017	0.1664	21.22
10	0.2139	0.1812	17.92
15	0.2326	0.2050	13.41
20	0.2419	0.2174	11.27
30	0.2473	0.2263	9.28
50	0.2362	0.2180	8.31

Table VI: Transmission Probability for ducts with concrete shielding.

Radius	1DWM	MCNP	% Dev.
8	0.009983	0.01314	-24.02
10	0.01799	0.02355	-23.60
15	0.04778	0.0609	-21.48
20	0.08730	0.1059	-17.52
30	0.1734	0.1972	-12.01
50	0.3228	0.3453	-6.51

Table VII: Reflection Probability for ducts with graphite shielding.

Radius	1WMD	MCNP	% Dev.
8	0.2239	0.1893	18.32
10	0.2484	0.2172	14.39
15	0.2879	0.2684	7.28
20	0.3083	0.2989	3.12
30	0.3203	0.3232	-0.93
50	0.3023	0.3135	-3.56

Table VIII: Transmission Probability for ducts with graphite shielding.

Radius	1DWM	MCNP	% Dev.
8	0.01931	0.01875	-3.03
10	0.03319	0.03408	-2.62
15	0.07872	0.08534	-7.75
20	0.1307	0.1431	-8.72
30	0.2289	0.2487	-7.94
50	0.3801	0.4025	-5.59

IV. MONTE CARLO-BASED LOGISTIC REGRESSION MODELS FOR NEUTRAL PARTICLE TRANSPORT IN DUCTS

Logistic regression is a standard method for modeling binary outcomes for a particular response variable and one, or several, explanatory variables and or mixing terms. Specifically, the response variable y_i, which corresponds to an underlying binomial distribution, can take on the values of 0 or 1. However, a linear regression model is not fitted to data $y = 0$ or 1, but rather to the probability that $y = 1$, [14]

$$p(y_i) = \text{logit}^{-1}(\beta_0 + \sum_{i=1}^{k} \beta_i x_i), \tag{115}$$

where βx_i is referred to as a linear predictor. The logit function is defined as the natural logarithm of an odds ratio,

$$\text{logit}(p) = \ln(\frac{p}{1-p}), \tag{116}$$

where p is the probability of an outcome [15]. The logit function is generally used to transform an 'S'-shaped curve into an approximate straight line and projects the curve's range corresponding to [0,1] onto $(-\infty\ ,\ +\infty)$ [16]. A logit regression model, therefore, can be expressed as $\text{logit(p)} = \beta_0 + \beta_1 x_1 + \cdots + \beta_k x_k$, which implies,

$$\frac{p}{1-p} = e^{\beta_0+\beta_1 x_1+\cdots+\beta_k x_k} \tag{117}$$

resulting in,

$$p = \frac{e^{\beta_0+\beta_1 x_1+\cdots+\beta_k x_k}}{1+e^{\beta_0+\beta_1 x_1+\cdots+\beta_k x_k}} = \text{logit}^{-1}(\beta_0 + \beta_1 x_1 + \cdots + \beta_k x_k) \tag{118}$$

As in the case of linear regression, the intercept β_0 represents the model assuming a zero value for other predictors. To provide a sense of how the logit scale works, specific values can be tested. For example:

• logit(0.5)=0, logit(0.75)= 1.09. What this implies is that an approximate increase of 1 on the logit scale will result in an increased probability of 25% (i.e. from 50% to 75%).

It should be noted— as seen in Fig. 3— that at either end of the scale probabilities are compacted, such that the range is kept between 0 and 1. As such, we can see that approximate increase of 1 at an extremity results in a different percent increase:

• logit(0.04)=-3.178, logit(0.1)= -2.197. In this case, an approximate increase of 1 on the logit scale results in the probability increasing by 6% (i.e. from 4% to 10%).

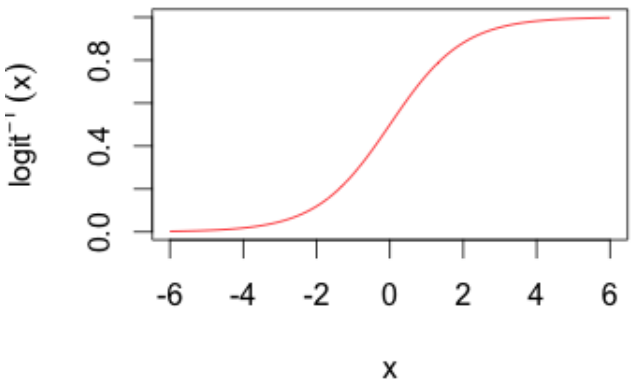

Fig. 3: The inverse-logit ("logistic") function, plotted in R. The curve is steepest at a probability of 0.5, with much more gradual change occurring at the edges.

IV.A. Maximum Likelihood Estimation

The coefficients of the model, $\mathbf{B} = \beta_{\mathbf{1}}, \ldots, \beta_{\mathbf{k}}$, are estimated by the method of maximum likelihood. If we define a likelihood function $L(\mathbf{B})$ as the joint probability of observing a set of collected data, the method of maximum likelihood is then applied by choosing the estimator of the set of parameters $\mathbf{B}$ which maximizes $L(\mathbf{B})$. [17]

The method of maximum likelihood can be explicitly demonstrated by being applied to a binomial distribution, where the likelihood function is expressed as

$$L(p) = c \times p^x \times (1-p)^{n-x} \tag{119}$$

where c is a constant, n = number of data points, x is a binary quantity equal to 1, and p is the probability of $x = 1$. In this case the maximum likelihood estimator is denoted as $\hat{p}$, and is obtained by solving

$$\frac{\partial L(p)}{\partial p} = 0, \tag{120}$$

for p. As such, $\hat{p}$ can be found as follows:

$$\begin{aligned} \frac{\partial L(p)}{\partial p} &= \frac{\partial (cp^x(1-p)^{n-x})}{\partial p} \\ &= xp^{x-1}(1-p)^{n-x} - p^x(n-x)(1-p)^{n-x-1} = 0, \end{aligned}$$

which implies,

$$\frac{n-x}{x} = \frac{p^{x-1}(1-p)^{n-x}}{p^x(1-p)^{n-x-1}} = \frac{1-p}{p},$$

thus, the maximum likelihood estimator for a binomial distribution is given as

$$\hat{p} = \frac{x}{n}. \tag{121}$$

Often finding the maximum likelihood estimator can be considerably simplified by taking the log of the likelihood function; this is a permissible alternative because the maximum of $L(\mathbf{B})$ will equal the maximum of $\ln(L(\mathbf{B}))$. This can easily be demonstrated by once more looking at the binomial distribution example,

$$\ln(L) = \ln(c) + x\ln(p) + (n-x)\ln(1-p), \tag{122}$$

where,

$$\frac{\partial \ln L}{\partial p} = \frac{x}{p} + \frac{n-x}{1-p} = 0, \tag{123}$$

which once more gives us $\hat{p} = \frac{x}{n}$.

A more general form of Eq. (121) is expressed as [17]

$$\frac{\partial \ln L(\mathbf{B})}{\partial \mathbf{B_i}} = 0, i = 0, 1, ..., k. \tag{124}$$

where k parameters corresponds to a set of k equations with k unknowns. These systems of equations must be solved iteratively by means of statistical software or packages in a programming language. In the case of logistic regression models, the likelihood function takes on one of two forms— an unconditional and conditional form. The unconditional form of the logistic likelihood function is expressed as the

product of the joint probability for dichotomous cases (0 vs 1), [17]

$$L_u = \prod_{i=1}^{j} p(\mathbf{x_i}) \prod_{\mathbf{i=j+1}}^{\mathbf{n}} [\mathbf{1} - \mathbf{p}(\mathbf{x_i})], \tag{125}$$

where,

$$p(\mathbf{x}) = \text{logistic model} = \frac{\mathbf{1}}{\mathbf{1} + \mathbf{e}^{-\beta_\mathbf{0} - \sum \beta_\mathbf{i} \mathbf{x_i}}}, \tag{126}$$

as such,

$$L_u = \frac{\prod_{i=1}^{n} e^{-\beta_0 - \sum \beta_i \mathbf{x_i}}}{\prod_{i=1}^{n} [1 + e^{-\beta_0 - \sum \beta_i \mathbf{x_i}}]}. \tag{127}$$

The conditional form of the logistic likelihood function is expressed as a ratio of the probability of observed data and the probability of all possible configurations of the given data, [17]

$$L_c = \frac{\prod_{i=1}^{j} p(\mathbf{x_i}) \prod_{\mathbf{i=j+1}}^{\mathbf{n}} [\mathbf{1} - \mathbf{p}(\mathbf{x_i})]}{\sum_u \{\prod_{l=1}^{j} p(\mathbf{x_{ul}}) \prod_{\mathbf{l=j}}^{\mathbf{n}} [\mathbf{1} - \mathbf{p}(\mathbf{x_{ul}})]\}}, \tag{128}$$

$$= \frac{\prod_{l=1}^{j} e^{\sum_{i=1}^{k} \beta_i \mathbf{x_{il}}}}{\sum_u [\prod_{l=1}^{j} e^{\sum_{i=1}^{k} \beta_i \mathbf{x_{lui}}}]}. \tag{129}$$

In its final form, the unconditional likelihood function for logistic models does not include the intercept (known as the nuisance parameter) β_0, and only coefficient estimates are calculated.

IV.B. Univariate Reflection and Transmission Models

In this work, multivariate logistic models are developed for circular ducts with iron, concrete, and graphite shielding, where an isotropically distributed neutron source is

located at the entrance ($z = 0$). The models are distinguished by shielding material and energy distribution of the neutron source. In particular, a Maxwellian distribution in the thermal-energy range is used as one source, and 14 MeV neutrons as a second source. Three explanatory variables are defined: duct radius (r), duct length (l), and thickness of shielding + inner duct radius (s), which are each defined over a unique range of values. The duct system configurations are similar to those of Ref. 6.

For neutral particles streaming in a duct system, p can be defined as the probability of reflection or transmission (where $y = 1$ corresponds to reflection/transmission, and $y = 0$ corresponds to no reflection/transmission). As such, logistic regression models can be applied, where reflection/transmission is the response variable and geometric features of a duct system serve as explanatory variables.

In order to build multivariate models, the relationship between the response variable (reflection/transmission) and each of the individual explanatory variables (r, L, S), while maintaining the remaining explanatory variables fixed, is tested. Each of the explanatory variables are plotted against the response variable, and univariate logistic regression models are created based on discernible correlations between the variables of interest.

In Fig. 4 the plots for radius versus reflection probability corresponds to a duct system with a thermal neutron source, for all listed shielding materials. In Fig. 5 the plots correspond to a duct system with graphite shielding, subject to a thermal and 14 MeV neutron source. In each case, the duct length is fixed to 100 cm, wall thickness is fixed to 20 cm, and the radius varies over a range of 0-500 cm. Figs. 4-5 indicate that models for each of the shielding (wall) materials can be built using

the same family of functions, differing only by specific factors. In Fig. 5 the plots indicate that the reflection probability for varying energy sources differ by specific factors (coefficients), but can be modeled by the same functions.

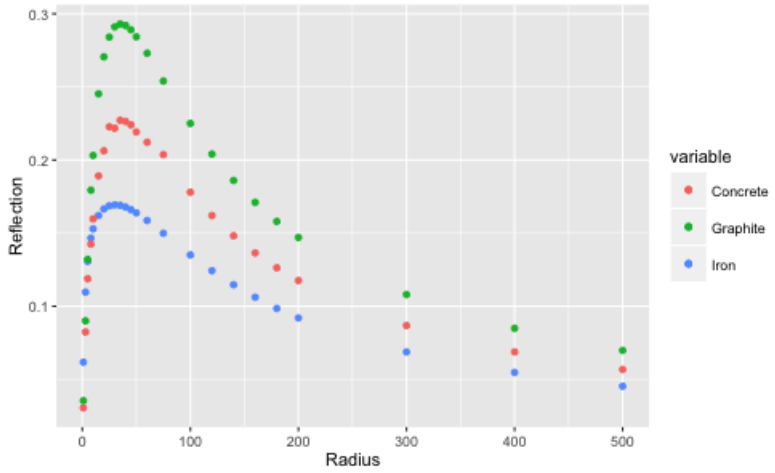

Fig. 4: Plot for radius vs reflection probability for ducts with a thermal neutron source.

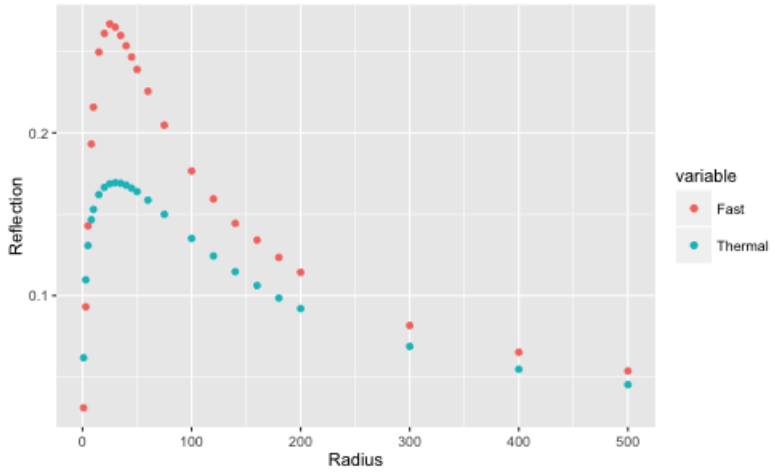

Fig. 5: Plot for radius vs reflection probability for a thermal neutron source and a 14 MeV (fast) neutron source, and graphite shielding.

The univariate logistic model is based on functions revealed by plotting our data versus a change in radius. Fig. 6 shows plots of candidate functions used to produce the logistic regression models for both reflection and transmission:

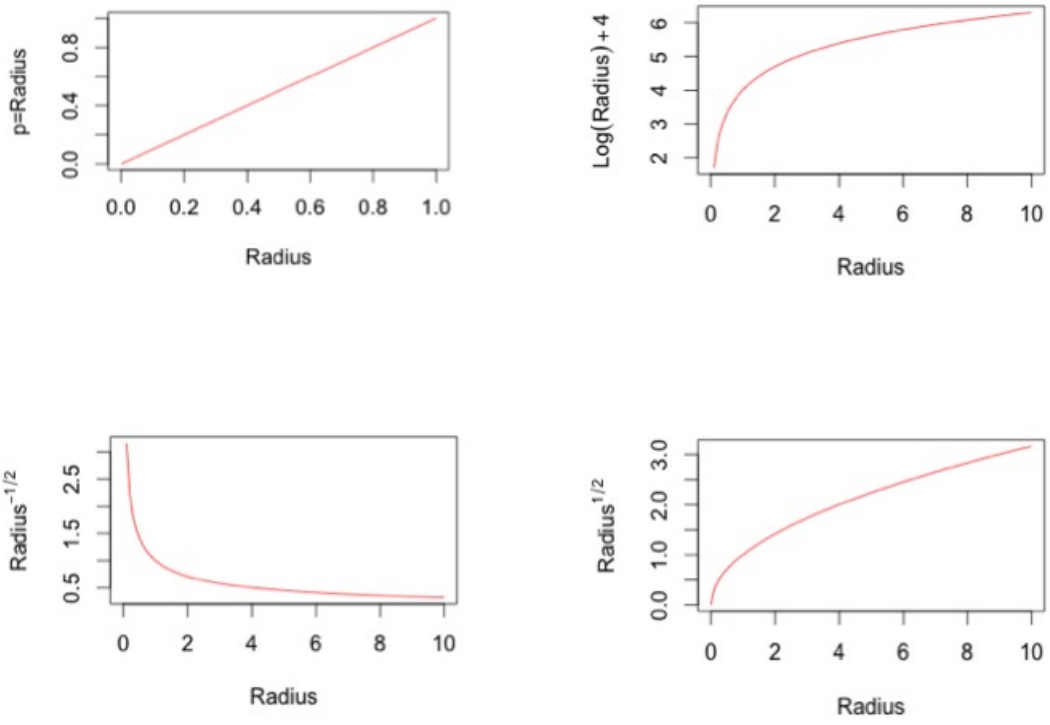

Fig. 6: Plots of candidate functions.

The candidate functions are $p = r, p = \mathrm{r}^{\frac{-1}{2}}, p = \mathrm{r}^{\frac{1}{2}}$ and $p = log(r) + 4$.

The generalized linear model (GLM), in R, [8] consists of three elements: a probability distribution, a linear predictor, and a link function. The probability distribution is from the exponential family, which includes the normal, binomial, Poisson, gamma,

and many other common distributions. The general expression for a distribution form is given by [15]

$$f(y|\theta,\tau) = h(y,\tau)exp((b(\theta)^T T(y) - A(\theta))/d(\tau)). \tag{130}$$

The functions h, b, T, A, and d are specified for the distribution, and τ, known as the dispersion parameters, is typically related to the variance. The linear predictor, η introduces the information about independent variables into the model,

$$\eta = X\beta, \tag{131}$$

where X is the design matrix and the vector β are the unknown coefficients that are to be determined. The link function relates the linear predictor to the mean of the probability distribution. For the examples included, the link is the logit function,

$$X\beta = ln(\mu\ (1-\mu)). \tag{132}$$

The model is fit using maximum likelihood estimation using iteratively re-weighted least squares (IRLS) regression. [18] IRLS is an optimization method that minimizes the squared error between the model and the true value.

Based on the plot in Fig. 2, a univariate model, presented (solely) for the case of iron shielding, for reflection probability (p) is input into R in the following general form, using the **glm** function,

$$\mathbf{Reflection.model} = \mathbf{glm}(\mathbf{p} \sim \mathbf{r} + \mathbf{logr} + \mathbf{rn05},$$
$$\mathbf{family} = \mathbf{binomial}, \mathbf{df}) \quad (133)$$

where $logr = Log(r) + 4$, and $rn05 = \mathrm{r}^{-\frac{1}{2}}$. R gives us the following synopsis for the reflection model:

Coefficients:

(**Intercept**)	**radius**	**logr**	**rn05**
0.138469	**− 0.003044**	**− 0.169622**	**− 2.267581**

Degree of Freedom : **23 Total** (**i.e. Null**; **20 Residual**)

Null Deviance : **0.3735**

Residual Deviance : **0.006296** **AIC** : **14.65**

The performance of a model can be evaluated by the values of the null and residual deviance. The deviance can be generally thought of as a measure of the lack of fit between a model and data. In particular, the null deviance indicates how well the response variable (p) is predicted by a model, if the model consisted solely of the intercept. The residual deviance indicates how well the response variable is predicted by a model when explanatory variables are included. Specifically, the residual deviance indicates whether or not the null hypothesis (i.e. the proposed model fits the data well) is true. If the value of the null deviance is relatively small it is an indicator that the null model explains the data well; likewise, a small value for residual deviance is an indicator that the proposed model explains the data well. If a proposed model improves upon the null model, the residual deviance

should be significantly smaller than the null deviance, as is the case for the reflection probability model (where a reduction of 0.3784 to 0.006296). In this context, the degree of freedom represents the number of ways the regression equation can vary (3) in addition to 20 residual terms.

The **AIC** (Akaike Information Criterion) term is a measure of the relative quality of candidate statistical models for a given set of data, with a penalty for the number of parameters (k). [15] AIC can be expressed as

$$AIC = 2k - 2\ ln(L), \tag{134}$$

where L is the maximum value of the likelihood function. The quality of the model as measured by the AIC, however, must be considered against reduction in the deviance. Table IX shows results for a number of candidate models, which demonstrate that while the change in AIC is relatively small between them, the accepted model leads to the most significant reduction in deviance. In each case the AIC values are on the same order, with the exception of the accepted model, which reduces the deviance by 2 orders of magnitude.

Table IX: A comparison of the candidate models for reflection probability. (**Accepted model.)

Formula	AIC	Null Dev.	Residual Dev.
Reflection $\sim r$	10.63	0.3735	0.1462
Reflection $\sim \log(r)$	10.60	0.3735	0.3381
Reflection $\sim r^{-1/2}$	10.60	0.3735	0.3707
Reflection $\sim r + r^{-1/2}$	12.64	0.3735	0.01234
Reflection $\sim r$+$\log(r)$	12.63	0.3735	0.04285
Reflection $\sim r^{-1/2} + \log(r)$	12.64	0.3735	0.04893
**Reflection $\sim r + r^{-1/2} + \log(r)$	14.64	0.3735	0.006296

Under the coefficients heading, R provides the maximum likelihood estimate for each coefficient. While the coefficients for logistic regression are open to interpretation, they are generally taken to mean the change in the log-odds of the result for one unit increases in the explanatory variables. Having defined the coefficients, a logistic model for reflection probability (p) can be explicitly stated as

$$\mathrm{p} = \mathrm{logit}^{-1}(0.1385 - 0.003044 * \mathrm{r} - 0.1696 * (\log(\mathrm{r}) + 4) - 2.2675 * \mathrm{r}^{\frac{-1}{2}}) \tag{135}$$

As an example, the analytic expression can be used to find the reflection probability for a duct of radius = 20 cm,

$$\mathrm{p} = \mathrm{logit}^{-1}(0.1385 - 0.003044 * (20) - 0.1696 * \log(20) + 4 - 2.2676 * 20^{\frac{-1}{2}})$$

$$= \frac{e^{(0.1385-0.003044*(20)-0.1696*(log(20)+4)-2.2676*20^{\frac{-1}{2}})}}{1+e^{(0.1385-0.003044*(20)-0.1696*(log(20)+4)-2.2676*20^{\frac{-1}{2}})}} = 0.1657.$$

The value predicted by the logistic model, $p = 0.1657$, can be compared to the actual value (as given by the data) $p_a = 0.1665$, which results in a percent difference = 0.46%. By use of the R function **Reflection.model$fitted** a table of predicted reflection probabilities corresponding to each of the radii in the data can be quickly produced, and compare them to actual values.

Table X: Comparison of the predicted and actual reflection probability.

Radius	Actual	Predicted	% Dev.
1	0.06177	0.05675	8.12
3	0.1096	0.1146	4.51
5	0.1307	0.1368	4.63
8	0.1466	0.15203	3.72
10	0.1529	0.1573	2.91
15	0.1621	0.1638	1.08
20	0.1666	0.1657	0.46
25	0.1689	0.1658	1.708
30	0.1693	0.1649	2.59
35	0.1689	0.16343	3.29
40	0.1678	0.1616	3.67
45	0.1659	0.1597	3.81
50	0.1638	0.1576	3.84

Table X continued: Comparison of predicted and actual reflection probability

Radius	Actual	Predicted	% Dev.
60	0.1586	0.1532	3.44
75	0.1499	0.1464	2.28
100	0.1351	0.1356	0.39
120	0.1243	0.1273	2.47
140	0.1147	0.1196	4.32
160	0.1062	0.1123	5.83
180	0.09847	0.1054	7.12
200	0.09200	0.09904	7.66
300	0.06874	0.07232	5.21
400	0.05471	0.05279	3.51
500	0.04529	0.03851	14.96
		Avg. % Dev.	4.231201

Table X indicates fairly good agreement between the model and the data, with the exception of the extreme points (where the duct entrance at 1 cm is 1/100 of the length, and at 500 cm where it is 5 times the length), which are difficult to accurately capture for physical models as well. Table X shows that the error values are highest at the extremes ($\sim$8.2 and $\sim$ 15 %), with an average error of $\sim$4.2 %.

Fig. 7 shows a plot of the data with an overlapping fit—that is, the regression equation expressed as a continuous function.

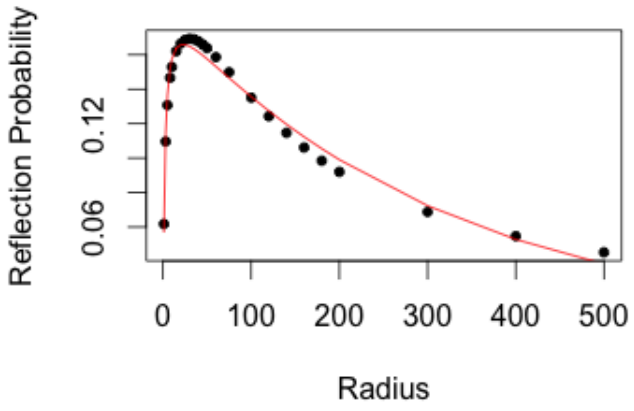

Fig. 7: Plot of transmission probability values with overlapping fit.

It should be noted that while the model fit featured in Fig. 7 is not unique, and can be derived using simpler alternatives, e.g. linear interpolation, regression has the intrinsic advantage of elucidating the relationship between dependent and independent variables. In particular, regression modeling establishes a function, or group of functions, which correlate the dependent and independent variables, and indicates the weighted importance of each function according to coefficients. For example, Eq. (136) itself produces the specific, quantifiable changes to reflection probability with respect to a changing radius, and indicates, via the coefficients, a heavy dependence on the inverse square root of the radius, and to a lesser degree the logarithm of the radius. The functions in this case, provide a clear indicator that as the radius becomes larger the reflection probability increases very slowly with respect to small radii values, and asymptotically approaches zero with respect to large radii values. The logarithm function is further indicative of a correlation between increases in

radius and wall attenuation; where the logarithmic intensity (I) of radiation incident upon a wall is attenuated according to $\ln(I_0)$ - μx, and μ and x are the attenuation coefficient and wall thickness. The form of Eq. (136), moreover, allows for higher order derivatives, and thus the calculation of sensitivities. That is, the first derivative can be calculated in order to measure how quickly reflection probability changes with respect to radius, while the second derivative can be calculated to measure how the rate of change with respect to radius is itself changing. Ultimately, the functions which constitute the univariate model indicate the radial features of the duct system which must be considered when developing a multivariate model.

While the fitted values are in good agreement with the given data, it is important to test the model against unseen data. To this end, the data was split into training and testing sets. The R function **mutate** [8] was used to add a new column, "sampled", to the existing data frame. Using the expanded data frame a method was developed, which allowed for continuous sampling of the data at random, automatically partitioning between training and testing sets after every run of the code. Specifically, a random number generator was used to partition and sample approximately 80% of the data to train the logistic model, while the remaining 20% was used as unseen data to test the logistic regression model. Table XI shows results for a random training set; while the error increases versus the fitted results, the model provides reasonable prediction values.

Table XI: Comparison of the predicted and actual reflection probability for a random test (unseen) data set.

Radius	Actual	Predicted	% Dev.
20	0.1665	0.1651	0.86
35	0.1689	0.1636	3.18
100	0.1351	0.1372	1.61
160	0.1061	0.1141	7.57
180	0.09847	0.1073	8.97
		Avg. % Dev.	4.44

Fig. 8 shows a plot of reflection probability predictions for the unseen/un-sampled data (corresponding to 0, red) against the predicted values for the training set (corresponding to 1, blue), with overlapping linear fits. In theory, the linear fits should have a slope ~ 1, indicating that the predicted values and the actual values are in very close agreement. The graph demonstrates the general trend of the reflection probability with respect to radius, and indicates fairly good agreement between both the predicted test and training points and the actual values.

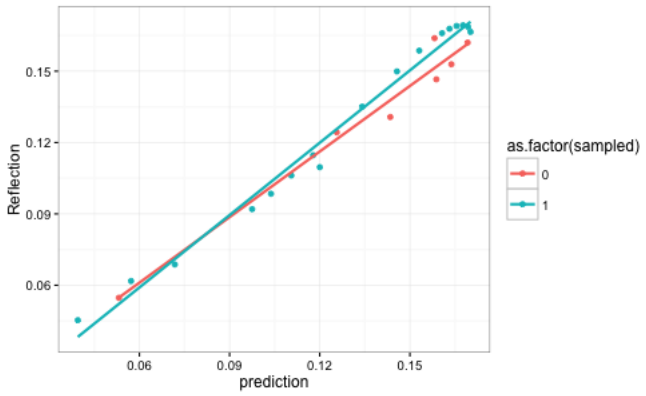

Fig. 8: Plot for predicted reflection probability for the training and test sets with overlapping linear fit.

Fig. 9 shows a plot for reflection probability for all 24 radii values, including both the training and test sets. The values corresponding to the test data (unseen data), are indicated by circular points versus triangular points for the training data.

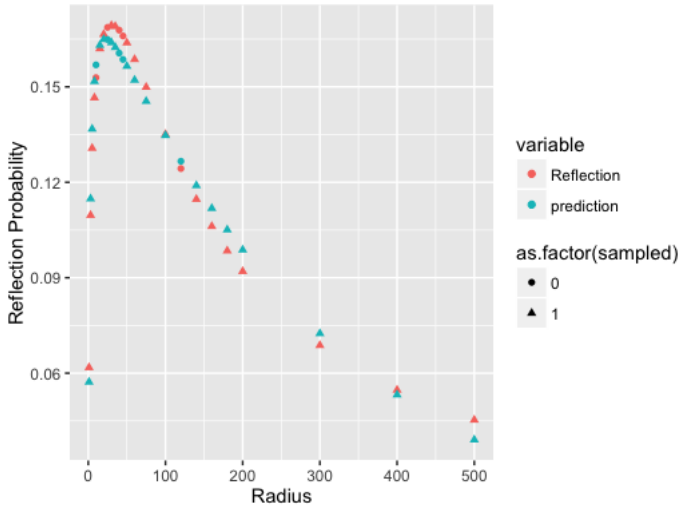

Fig. 9: Plots for predicted and actual reflection probability versus radius, for both test and training sets.

Using the methods applied to the reflection probability data, a univariate logistic regression model was developed for transmission probability (t) in a duct. The data is initially plotted according to shielding material and energy source (see Figs. 10-11).

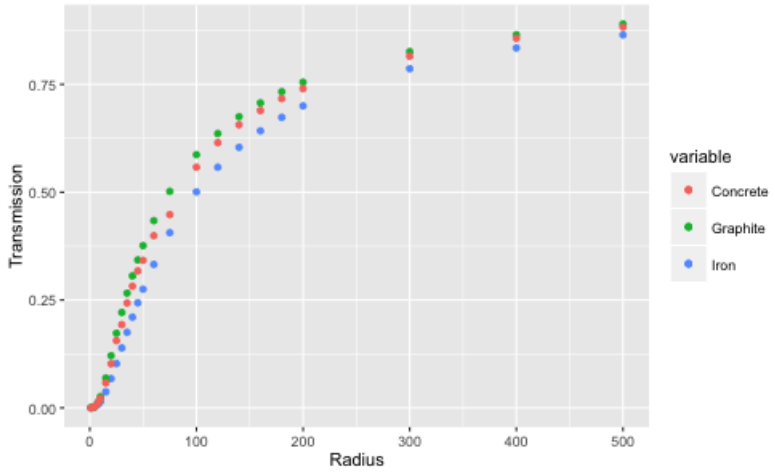

Fig. 10: Plot for radius versus transmission probability for three different materials, with a thermal neutron source.

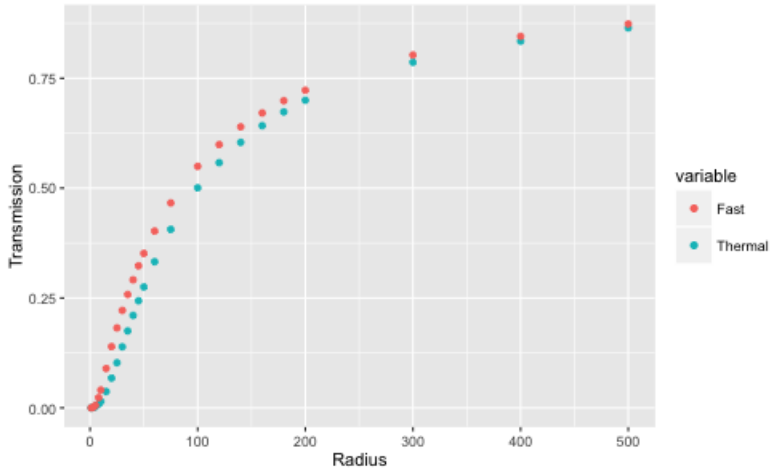

Fig. 11: Plot for radius versus transmission probability for a thermal neutron source and a fast (14 MeV) neutron source.

Specifically, the model is applied to a 100 cm long duct with a thermal neutron source at the entrance, iron shielding, and varying radius. Plotting the transmission probability values against the radius for ducts with a thermal source (iron, concrete, and graphite shielding), and a 14 MeV source (iron shielding),as seen in Figs. 10-11, a comparison is made to the candidate functions in Fig. 6 to derive a number of competing logistic models. Table XII shows a comparison of several logistic models for the transmission probability,using the metrics AIC, Null, and Residual deviance to choose the optimal model.

Table XII: A comparison of the candidate models for reflection probability. (**Accepted model.)

Formula	AIC	Null Dev.	Residual Dev.
Transmission $\sim r$	19.17	10.72	2.7228
Transmission $\sim \log(r)$	15.60	10.72	0.1023
Transmission $\sim r^{\frac{1}{2}}$	16.51	10.72	1.03
Transmission $\sim r + r^{\frac{1}{2}}$	16.98	10.72	0.22
Transmission $\sim r$+$\log(r)$	12.63	0.3735	0.042
Transmission $\sim r^{\frac{1}{2}} + \log(r)$	17.48	10.72	0.01772
**Transmission $\sim r + r^{\frac{1}{2}} + \log(r)$	19.74	10.72	0.001704

Based on the results listed in Table XII the optimal glm transmission probability

model is expressed as

$$\textbf{Transmission.model} = \textbf{glm(t} \sim \textbf{r} + \textbf{logr} + \textbf{r05,} \\ \textbf{family} = \textbf{binomial,df)}, \quad (136)$$

where $\mathrm{r05} = \mathrm{r}^{\frac{1}{2}}$. Having defined the coefficients, a logistic model transmission probability can be explicitly stated as

$$\mathrm{t} = \mathrm{logit}^{-1}(-21.094505 + 0.007988 * \mathrm{r} \\ + 2.929327 * (\log(\mathrm{r}) + 4) - 0.488600 * \mathrm{r}^{\frac{1}{2}}). \quad (137)$$

As with the reflection probability model, the R function **Transmission.model$fitted** can be used to produce a table of predicted transmission probabilities, corresponding to each of the radii in the data, and compare them to actual values.

Table XIII: Comparison of the predicted and actual reflection probability.

Radius	Actual	Predicted	% Dev.
1	0.000106	0.00005233	50.62
3	0.000995	0.0009282	6.71
5	0.002903	0.003285	13.14
8	0.008744	.000013	13.37
10	0.01473	.01634	10.90
15	0.03715	.03853	3.70
20	0.06778	.06742	0.53
25	0.1027	0.1005	2.15

Table XIII continued: Comparison of the predicted and actual reflection probability.

Radius	Actual	Predicted	% Dev.
30	0.1389	0.1358	2.28
35	0.1751	0.1717	1.92
40	0.2103	0.2072	1.50
45	0.2436	0.2415	0.88
50	0.2751	0.2743	0.32
60	0.3326	0.3343	0.49
75	0.4061	0.4104	1.06
100	0.5007	0.5064	1.13
120	0.5579	0.5629	0.89
140	0.6040	0.6072	0.51
160	0.6421	0.6428	0.095
180	0.6734	0.6720	0.21
200	0.6999	0.6966	0.48
300	0.7863	0.7798	0.83
400	0.8343	0.8316	0.33
500	0.8646	0.8695	0.55
		Avg. % Dev.	4.231201

Despite very large error for ducts with radius = 1 cm, the transmission probability model performs extremely well, giving an average percent error under 5%. In particular, for radii $>$ 10 cm the error rate quickly approaches zero. With a total duct length of 100 cm it is difficult to model for very small radii. It is expected that for a duct with a small entrance, subject to a thermal neutron source, most neutrons will be absorbed by the shielding or reflected out of the duct, producing a transmission that is essentially equal to zero. Particularly for natural iron shielding,

which has a relatively high thermal absorption cross-section ($\sigma_a = 4.6 \cdot 10^{-2}\ b$) and a thermal scattering cross-section of zero, it is expected that a very large fraction of neutrons will be absorbed. At very large radii (> 100 cm), the transmission probability increases very gradually, as it reaches a constant value (of $t = 1$), and the error is therefore virtually non-existent. In Fig. 12, below, we see a plot of transmission probability data with an overlapping fit—the regression equation expressed as a constant function—which match extremely well.

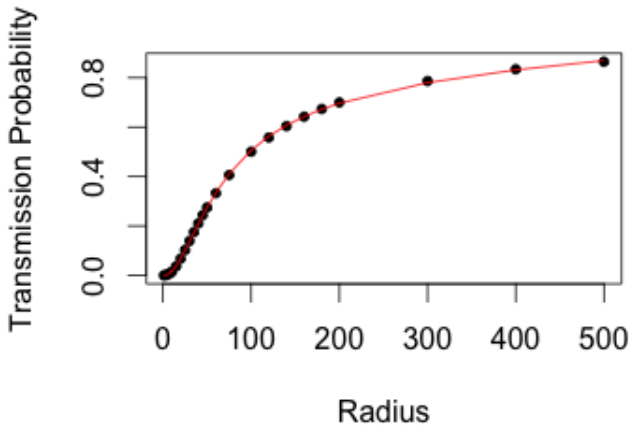

Fig. 12: Plot of reflection probability values with overlapping fit.

Using the same method applied to the reflection probability model, we partition our data and use the training set to develop the transmission probability model and subsequently make predictions for a random set of test (unseen) data.

Table XIV: Comparison of the predicted and actual reflection probability for a random test (unseen) data set.

Radius	Actual	Predicted	% Dev.
20	0.1665	0.1651	0.86
35	0.1689	0.1636	3.18
100	0.1351	0.1372	1.61
160	0.1061	0.1141	7.57
180	0.09847	0.1073	8.97
		Avg. %Dev.	4.44

As indicated by Table XIV the transmission model for iron ducts performs extremely well on unseen data, resulting in a mean percent of error of $\sim$1.74. However, given that the randomly chosen test set excludes small radii values, it is expected that the percent error would increase notably if they were included. Fig. 13 shows transmission probability predictions plotted against actual values, for both the training and test data with overlapping linear fits.

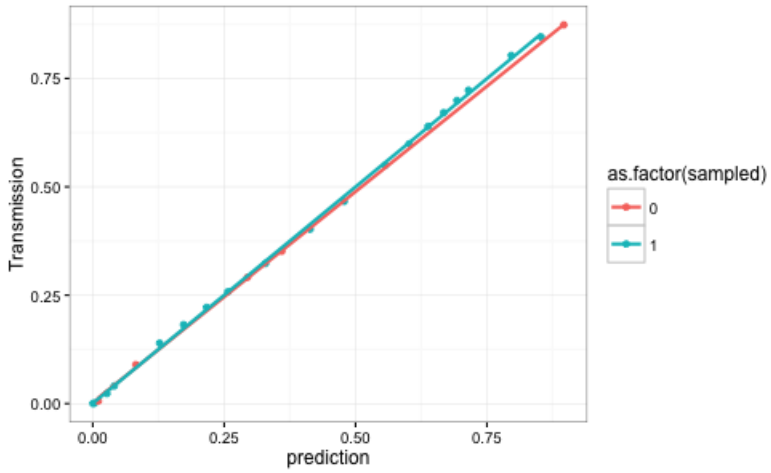

Fig. 13: Predicted transmission probability.

Fig. 14 shows radius plotted versus transmission probabilities for all 24 radii values, including both the training and test sets. The values corresponding to the test data (unseen data), are indicated by circular points, versus triangular points for the training data.

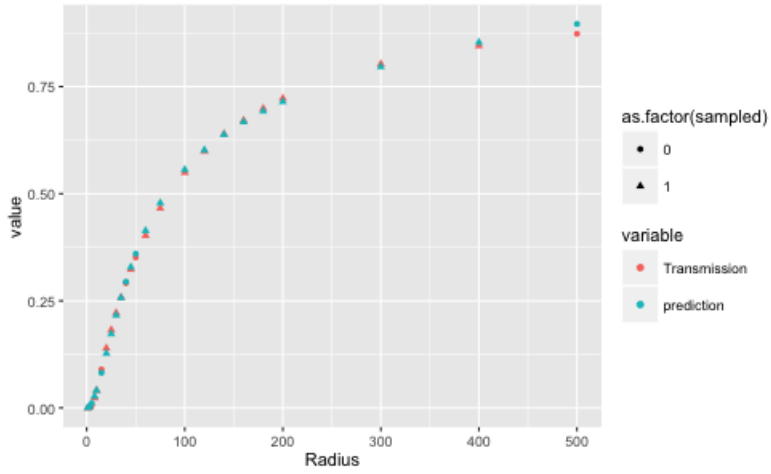

Fig. 14: Plots for the predicted and actual transmission probability versus radius, for both test and training sets.

Using the methods applied to the derivation of reflection and transmission models with respect to a change in radius, we derive univariate models accounting for changes in length and shield thickness. Below (see Figs. 15-16) are plots of reflection and transmission data, for ducts with a thermal source located at the entrance, versus length and shield upon which our models are based.

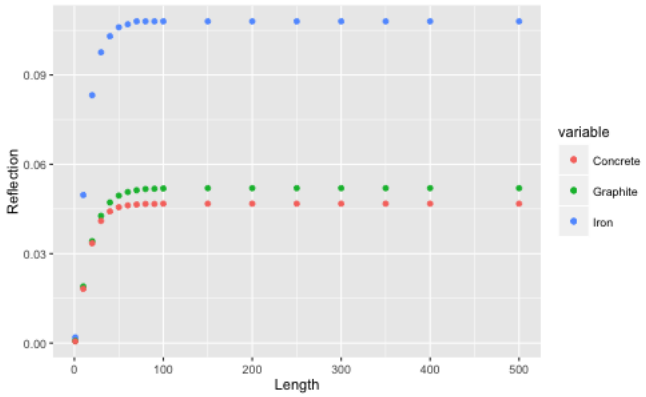

Fig. 15: Reflection probability vs length, for iron (black),concrete (red), and graphite (purple) ducts.

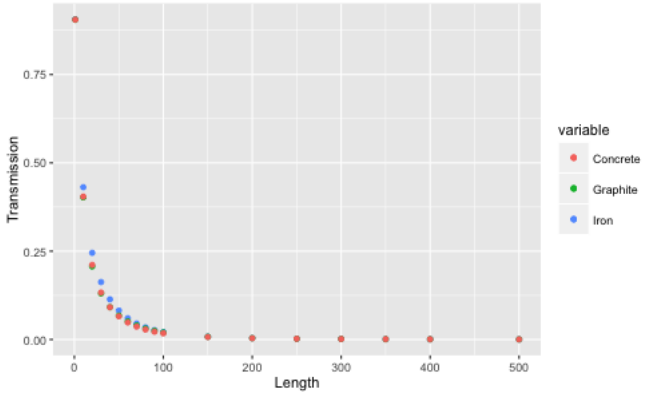

Fig. 16: Transmission probability vs length, for iron (black),concrete (red), and graphite (purple) ducts.

Given the data plotted in Fig. 15, the logistic regression model for length versus reflection probability, where the radius is kept fixed to 10 cm and the shield is kept fixed to 20 cm, is summarized as follows:

Coefficients:

(**Intercept**)	**length**	**logL**	**ln05**
0.1331855	**0.0003655**	**− 0.3430147**	**− 6.8418396**

Degree of Freedom : **13 Total** (**i.e. Null**; **10 Residual**)

Null Deviance : **0.2348 Residual Deviance** : **0.001762 AIC** : **11.67**.

The explicit regression equation for reflection probability for ducts with iron shielding, with length as an independent variable, can therefore be expressed as

$$\mathrm{p} = \mathrm{logit}^{-1}(0.1331855 + 0.0003655 * \mathrm{L} - 0.3430147 * \log(\mathrm{L}) - 6.8418396 * \mathrm{L}^{\frac{-1}{2}}). \quad (138)$$

By using the R **fitted** [15] function, the reflection probabilities calculated using Eq. (138) can be compared directly to our actual data values. Table XV provides predictions corresponding to the entire data set. It should be noted that predictions for very small values of length ($L < 10$), high errors are expected as this would represent a physical case where the radius is considerably larger than the duct length and the reflection probability would be very near zero. Likewise, for very large values of length ($L > 50$) it is expected that the reflection probability would approach a constant as the transmission probability approaches zero. In the latter case, most if not all of the neutrons would have scattered out of the system (through the duct entrance or the shield) or been absorbed before reaching the duct exit. As such, taking a test set of data which more accurately represents realistic physical systems

(i.e. where the ratio $L/r >> 1$), would lead to a considerably lower mean error. In this instance, a better indicator of the accuracy of the model is the median, where the median percent difference, corresponding to the data in Table XV, is 1.31 %.

Table XV: Comparison of the predicted and actual reflection probability.

Radius	Actual	Predicted	% Dev.
1	0.0019	0.001219	35.82
10	0.0497	0.05643	13.55
20	0.0832	0.08188	1.57
30	0.0976	0.09349	4.20
40	0.1030	0.09981	3.09
50	0.1060	0.1035	2.27
60	0.1070	0.1059	0.96
70	0.1080	0.1075	0.44
80	0.1080	0.1085	0.51
90	0.1080	0.1092	1.14
100	0.1080	0.1096	1.54
150	0.1080	0.1101	1.97
200	0.1080	0.1095	1.47
250	0.1080	0.1088	0.82
300	0.1080	0.1082	0.23
350	0.1080	0.1077	0.23
400	0.1080	0.1073	0.57
500	0.1080	0.1070	0.92

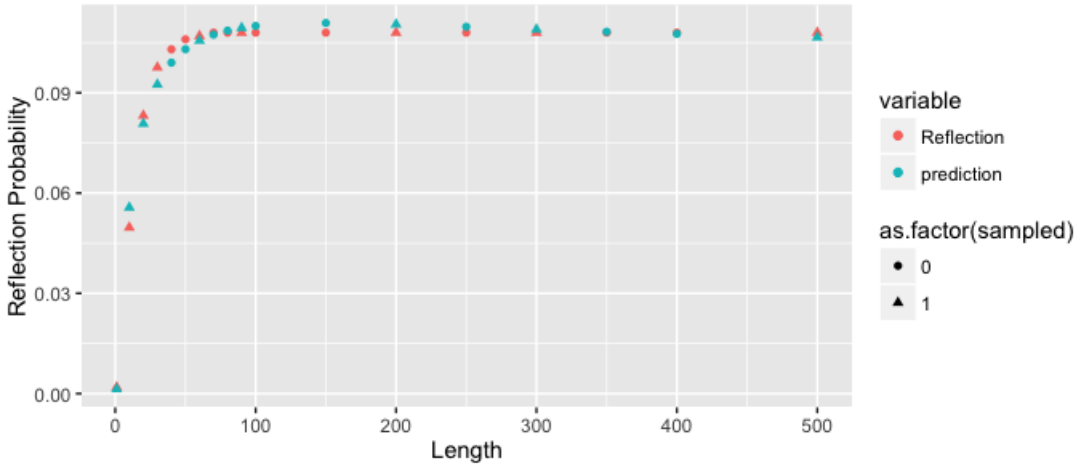

Fig. 17: Reflection probability versus length.

In Fig. 17 the reflection probability and model predictions are plotted versus changing length, for both training and test sets. Test set values are indicted by circles and training set values are indicated by triangles. Fig. 18 provides the same information as Fig. 17 for the transmission probability with respect to changing length. An analytical expression for transmission probability (t) is given as

$$\mathbf{t}(L) = \text{logit}^{-1}(2.40638 - 0.003313 * \text{L} - 0.157712 * \log(\text{L}) - 0.918251 * \text{L}^{\frac{1}{2}}). \quad (139)$$

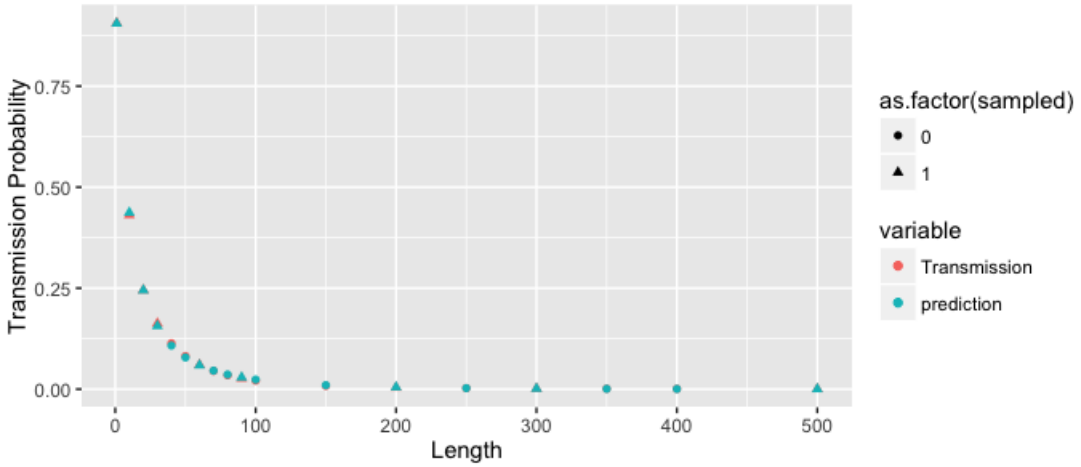

Fig. 18: Transmission probability versus length.

The median percent difference, between actual values and those predicted using Eq. (139), is 4.81%.

Fig. 19 shows the change in reflection probability with respect to shielding thickness (in cm), for concrete, graphite, and iron. The plot indicates that for concrete the reflection probability reaches a constant value at approximately 20 cm of shielding, while the same is true for graphite and iron at approximately 40 cm. Notably, the plot also indicates that regardless of the shielding thickness the reflection probability is considerably higher in iron ducts, while the probabilities are comparable for graphite and concrete ducts, except at large thickness values. Fig. 20 indicates that the same trends do not hold for the transmission probability. The transmission probability continues to increase beyond 50 cm for both iron and graphite; only concrete quickly reaches a constant value, once again at approximately 20 cm.

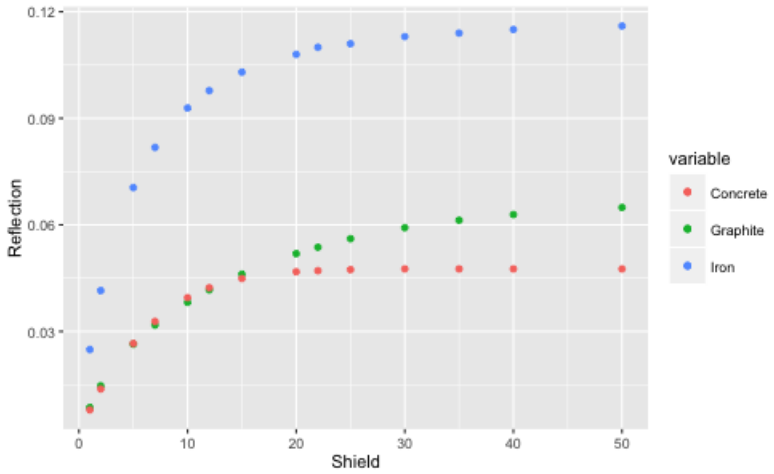

Fig. 19: Reflection probability versus shield thickness.

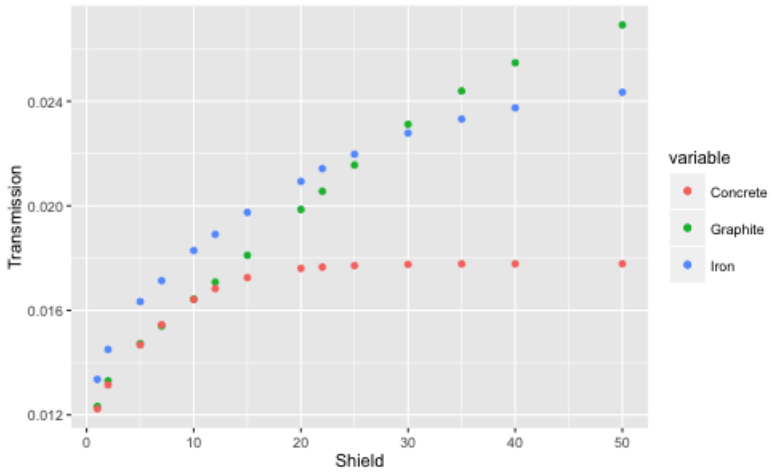

Fig. 20: Transmission probability versus shield thickness.

Based on Figs. 19-20, and repeating the model selection process, an analytical

expression for reflection and transmission probability (p and t, respectively) are given as:

$$\mathrm{p}(s) = \mathrm{logit}^{-1}(-3.05056 + 0.02428 * \mathbf{s} + 1.11070 * \log(\mathbf{s}) - 0.64197 * \mathbf{s}^{\frac{1}{2}}), \quad (140)$$

$$\mathrm{t}(s) = \mathrm{logit}^{-1}(-4.482481 - 0.011977 * \mathbf{s} - 0.003052 * \log(\mathbf{s}) - 0.198733 * \mathbf{s}^{\frac{1}{2}}). \quad (141)$$

The median percent deviation, between actual reflection probability values and those predicted using Eq. (141), mpd= 0.0894%; for actual transmission probability versus predicted values, mpd = 0.2772%. In Figs. 21-22 actual values as well as the predicted reflection and transmission probability, for both training and test sets, are plotted with respect to shielding thickness.

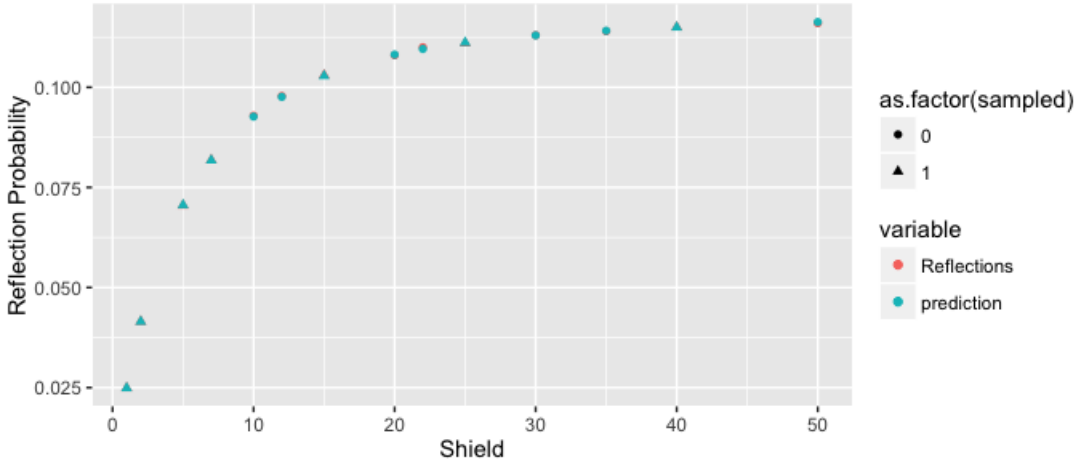

Fig. 21: Reflection probability versus shield thickness.

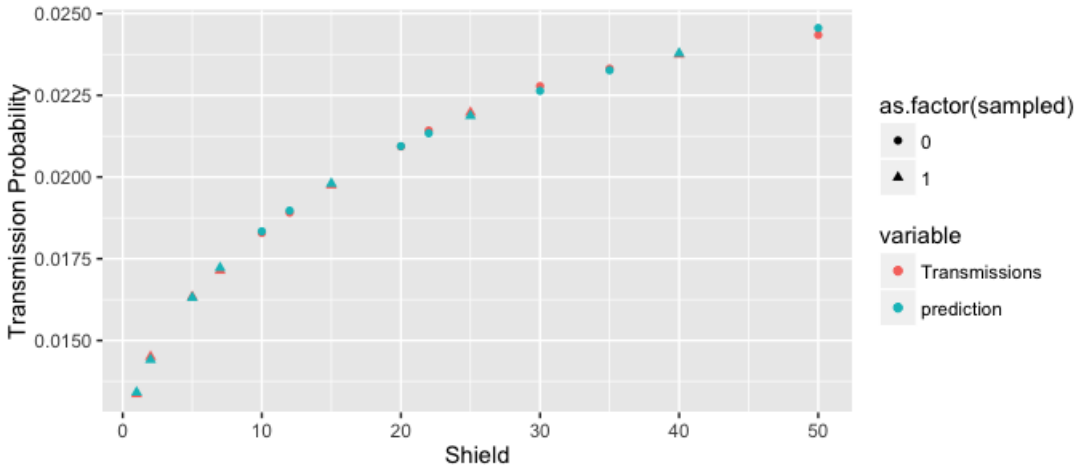

Fig. 22: Transmission probability versus shield thickness.

IV.C. Multivariate Reflection and Transmission Models

Latin Hypercube Sampling (LHS) is used to ensure that samples are evenly distributed over a defined sample space. [19] With 100 data points, the sample space is partitioned into cubes over a $5 \times 5 \times 4$ (*Length* $\times$ *Radius* $\times$ *Shield*) grid. LHS ensures that each cube contains at least one sample point.

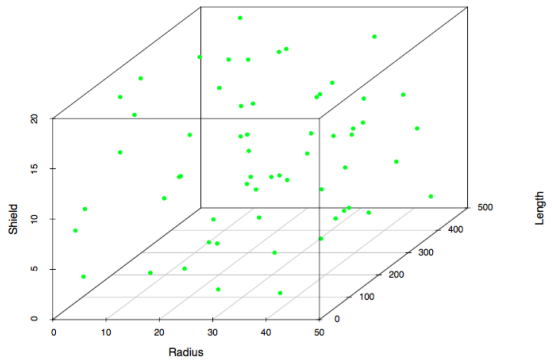

Fig. 23: Sample space partitioned by LHS.

Based on the univariate models, numerous candidate models and corresponding diagnostic parameters are compared in order to find the optimal model. Table XVI shows a number of candidate models considered, as well as their corresponding AIC, residual deviance, and the average percent error of predictions for all 100 data values.

Table XVI: Candidate models for iron ducts with a thermal source.

Model	AIC	R. D.	AE%
$RP \sim logit^{-1}(r^{\frac{-1}{2}} + L^{\frac{-1}{2}} + Log(S) + Log(L) + Log(r))$	45.59	0.1119	6.08
$RP \sim logit^{-1}(r^{\frac{-1}{2}} + L^{\frac{-1}{2}} + Log(S) + Log(L * r))$	43.59	0.1119	6.06
$RP \sim logit^{-1}(S + L^{\frac{-1}{2}} + Log(S) + Log(L) + Log(r))$	45.59	0.1724	6.86
$T \sim logit^{-1}(r^{\frac{1}{2}} + L^{\frac{-1}{2}} + Log(S) + Log(L) + Log(r) + Log(r) * Log(L) * Log(S))$	28.12	0.0571	10.26
$T \sim logit^{-1}(r^{\frac{1}{2}} + L^{\frac{-1}{2}} + Log(S) + Log(L) + Log(r))$	25.28	0.148	40.57
$T \sim logit^{-1}(r^{\frac{-1}{2}} + L^{\frac{-1}{2}} + Log(S) + Log(L) + Log(r) + Log(r) * Log(L) * Log(S))$	28.12	0.0518	9.60

where, r: Radius, L:Length, S:Shield, RP: Reflection Probability, T: Transmission Probability. Based on the results in Table XVI, an analytical expression for the reflection probability (p) for iron ducts, subject to a thermal neutron source, is given

as

$$p(r, L, S) = \text{logit}^{-1}(0.8724 + 0.1013 * Log(S) - 0.2263 * Log(r * L) - 2.182 * r^{\frac{-1}{2}} - 6.74 * L^{\frac{-1}{2}}). \quad (142)$$

Generally, in linear regression, the coefficients of a model indicate the effect of each of the explanatory variables. However, in multivariate logistic regression models, the logit scale makes interpreting a variable's impact more complicated. In Eq. (142) the coefficients indicate that the length of the duct has the greatest impact on the reflection probability; that is, increasing the duct length appears to reduce the reflection probability at the fastest rate. However, in order to quantify and confirm the effect of each of the explanatory variables, predicted difference must be calculated. The predictive different in probabilities between two cases, which differ only by a change in a single parameter is defined as [14]

$$\delta(u', u, v, \beta) = P(y = 1|u', v, \beta) - P(y = 1|u, v, \beta), \quad (143)$$

where u is the input of interest, and v is the vector consisting of all other inputs. The average predictive difference can therefore be calculated as [14]

$$\Delta(u, u') = \frac{1}{n} \sum_{i=1}^{n} \delta(u, u', v_i, \beta). \quad (144)$$

For example, if two of the explanatory variables for the system are held constant, an increase in 10 cm (10 cm - 20 cm) for the third variable gives an average predictive difference for each of the duct parameters can be calculated as

$$\Delta(L, L_{10}) = 0.03627$$

$$\Delta(r, r_{10}) = 0.00596$$

$$\Delta(S, S_{10}) = 0.00846$$

The predictive differences confirm that changes in length, for iron ducts subject to a thermal source, has by far the largest effect on the reflection probability— where on average a change of 10 cm to 20 cm in length leads to an approximately 3.6% increase in reflection probability. The predictive differences also show that small changes in the radius and shielding lead to comparable changes in reflection probability. The R code to calculate predictive change in length (for example) can be input as follows:

c <− coefficients(Reflection.model)

L0 <− 10

L1 <− 20

u1 <− log(L0*r)

u0 <− log(L1*r)

LogS <− log(S) R.I <− r∧(-0.5)

delta = invlogit(c[1] + c[2]LogS +c[3]*u1 + c[4]*R.I + c[5]*L1∧(-0.5)) - invlogit(c[1] + c[2]LogS +c[3]*u0 + c[4]*R.I + c[5]*L0∧(-0.5))

print(mean(delta))

Testing for a much larger change in the parameters, for example a 100 cm change, leads to $\Delta_{L100} = 0.09003, \Delta_{r100} = -0.00775, \text{and} \Delta_{S100} = 0.03111$. With much larger changes in the explanatory variables, changes in length remains the dominant effect; however, changes in radius now lead to a small decrease in reflection probability, and changes in shielding thickness now have a larger positive effect on the reflection

probability.

The appearance of the $L * R$ term in Eq. (142) allows us to test the impact of increasing the duct's surface area ($2\pi r * L$). In this case, the length and radius are simultaneously increased (thereby increasing the surface area), while keeping the shielding thickness constant, and the predictive change is calculated. The predictive changes, when increasing the surface area by a factor of 4 ($L, r = 10 -> L = r = 20$) and 100 ($L, r = 10 -> L, r = 100$), are $\Delta_{4SA} = 0.04059, \Delta_{100SA} = 0.08241$. The predictive changes indicate that increasing the surface area gradually increases the reflection probability, which is consistent with the previous results; while increases in the size of the duct radius eventually have a negative effect, it is relatively negligible compared to the positive effect of length increases.

Table XVII: Predicted reflection probability for a random test set.

Radius	Length	Shield	Actual	Predict.	%Dev.
40	271	53	0.174994	0.1704271	2.60
12	412	37	0.157366	0.1612695	2.48
35	189	64	0.173483	0.1741763	0.39
13	105	25	0.159038	0.1547263	2.71
9	405	15	0.149805	0.1453504	2.97
46	168	59	0.173936	0.1704594	1.99
36	405	57	0.174199	0.1698746	2.48

Table XVII continued: Predicted reflection probability for a random test set.

Radius	Length	Shield	Actual	Predict.	%Dev.
17	436	50	0.164445	0.1679748	2.14
9	46	40	0.149525	0.1372536	8.20
31	115	59	0.170606	0.1699671	0.37
50	318	70	0.176548	0.1717505	2.71
16	222	22	0.162994	0.1594295	2.18
33	193	37	0.169757	0.1667080	1.79
34	255	50	0.173526	0.1708257	1.55
17	347	18	0.110458	0.1556633	40.92
8	18	39	0.136986	0.0961766	29.79
22	60	48	0.162911	0.1549042	4.91

In Table XVII predictions are listed for random test points, where the original data has been partitioned into training (80 %) and test (20 %) sets. While the the predictions are generally accurate to a high degree, the mean percent deviation (6.06%) is skewed by outliers; as such, the median percent deviation (2.55 %) gives a better representation of the model's accuracy. Figs. 24-25, where both test and training predictions are included, provide visual confirmation of how well the model performs; the linear fits for both sampled and un-sampled values have a slope close to 1, while the error terms in Fig. 25 are largely clustered around 0.

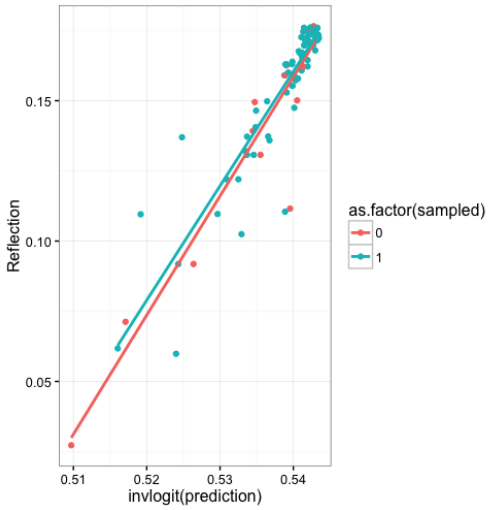

Fig. 24: Linear fit for actual and predicted reflection probability.

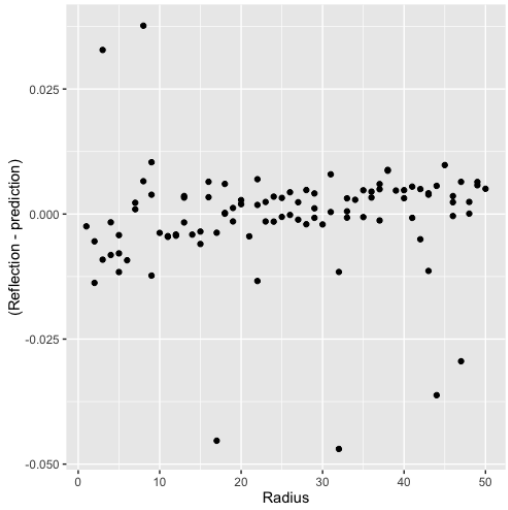

Fig. 25: Error terms for reflection probability.

An analytical expression for transmission probability (t), for iron ducts subject to a thermal neutron source, is given as:

$$t(r, L, S) = \text{logit}^{-1}(15.1484 - 0.7768 * Log(S) - 3.1584 * Log(L) - 0.2383 * Log(r) - 8.8674 * r^{\frac{-1}{2}} - 9.5535 * L^{\frac{-1}{2}} + 0.0635 * Log(r) * Log(L) * Log(S)). \quad (145)$$

The model coefficients in Eq. (146) indicate that, like the reflection probability model, the duct length has the largest impact on the probability of transmission. In this case, however, the effect of the duct length is more pronounced. Calculating the predictive differences, once more for increases of 10 and 100 cm, gives

$$\Delta(L, L_{10}) = -0.1485, \quad \Delta(L, L_{100}) = -0.5794$$

$$\Delta(r, r_{10}) = 0.0368, \quad \Delta(r, r_{100}) = 0.2459$$
$$\Delta(S, S_{10}) = 0.0031, \quad \Delta(S, S_{100}) = 0.0168$$

The predictive difference results are intuitively consistent with the physical behavior of radiation in ducts. As the length of the ducts get larger, the neutrons penetrate the walls and are absorbed or scattered out to a greater degree, reducing the transmission probability in the process; therefore, as expected, the transmission probability quickly approaches zero as large increments in the duct's length are made. While both increasing the radius and shielding lead to increases in the transmission probability, it is clear that there combined effects are negligible compared to changes in length; particularly as the duct lengths get very large.

Table XVIII: Predicted transmission probability for a random test set.

Radius	Length	Shield	Actual	Predict.	%Dev.
40	271	53	0.03616	0.03622	0.17
12	412	37	0.000939	0.001042	10.98
35	189	64	0.05863	0.05967	1.78
13	105	25	0.02427	0.02623	8.07
9	405	15	0.000529	0.0004984	5.77
46	168	59	0.1204	0.1111	7.83
36	405	57	0.0113	0.01423	25.86
17	436	50	0.001698	0.002255	32.84
9	46	40	0.06401	0.06141	4.06
31	115	59	0.1171	0.1102	5.83

Table XVIII continued: Predicted transmission probability for a random test set.

Radius	Length	Shield	Actual	Predict.	%Dev.
50	318	70	0.04171	0.04779	14.58
16	222	22	0.006902	0.007427	7.60
33	193	37	0.04925	0.04214	14.44
34	255	50	0.02891	0.02938	1.62
17	347	18	0.002683	0.002819	5.08
8	18	39	0.2311	0.2124	8.09
22	60	48	0.1856	0.1765	4.90

Table XVIII provides the percent deviation for a random test set, and indicates that while the median percent deviation is highly accurate, the mean is skewed by outliers. Figs. 26-27, which included both test and training set predictions, are consistent with the results of Table XVIII. In Fig. 26 the linear fits for both sampled and un-sampled data have slopes of almost exactly one; Fig. 27 shows that while a significant number of outliers are present, the vast majority of error terms are tightly clustered around a value of 0 (to a greater degree than the reflection probability model).

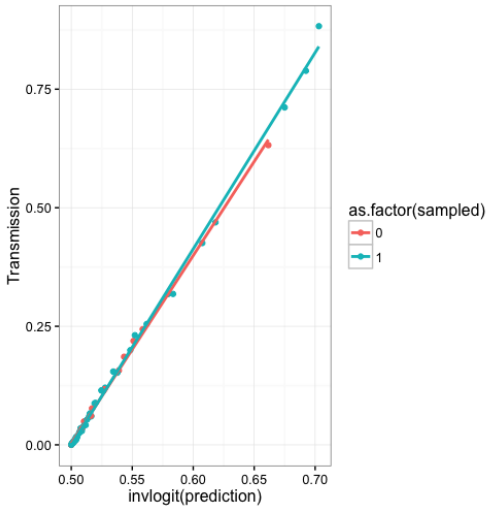

Fig. 26: Linear fit for actual and predicted transmission probability.

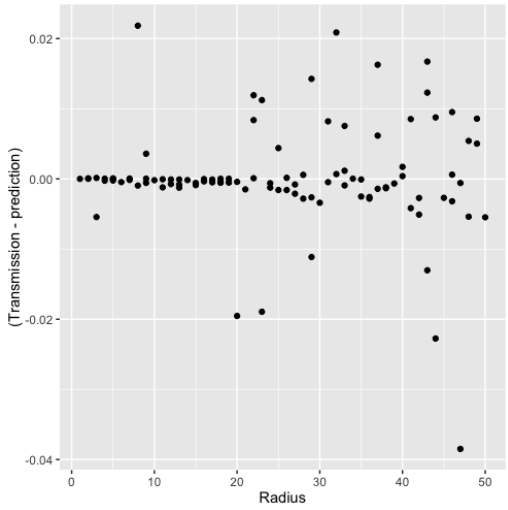

Fig. 27: Error Terms for transmission probability.

Given that the remainder of the reflection and transmission probability models, regardless of shielding material or source, have the same form as the iron duct models, they are presented without analysis in the following section, in order to avoid repetition. However, exceptions are made for graphite ducts subject to a 14 MeV neutron source, where visualizations are provided for the predictions of both the test and training set, via a linear fit and error term figures; for concrete ducts, subject to a 14 MeV neutron source, visualizations are provided for reflection and transmission probability predictions, as plots with respect to length in the former case, and with respect to shielding in the ladder case. The reasoning behind the analysis for thermal iron models is wholly applicable to the remaining models. A summary of the mean and median percent deviation for each of the models is presented at the conclusion of following section.

IV.D. Multivariate Models: Summary of Results

An analytical expression for the reflection probability (p) of graphite ducts, subject to a 14 MeV neutron source, is given as

$$p(r, L, S) = \text{logit}^{-1}(17.62762 - 0.0266 * r - 4.16652 * Log(S) - 0.30629 * Log(L * r) - 4.68217 * r^{\frac{-1}{2}} - 11.20193 * L^{\frac{-1}{2}} + 29.1673 * S^{\frac{-1}{2}}). \quad (146)$$

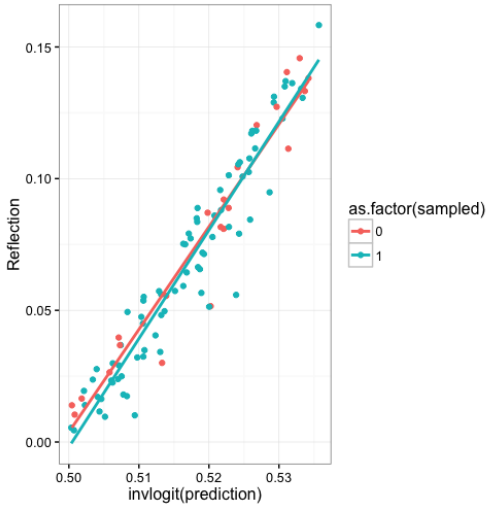

Fig. 28: Linear fit for actual and predicted reflection probability.

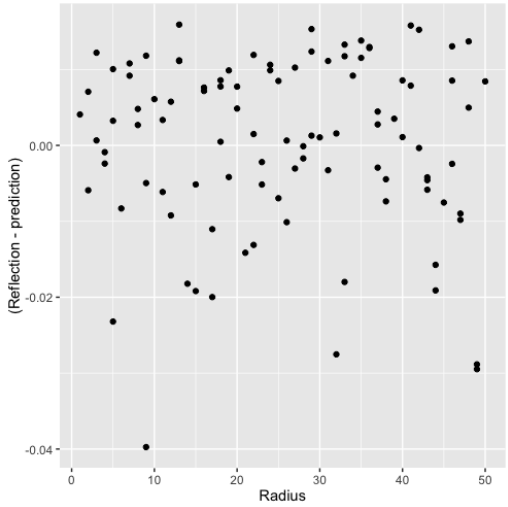

Fig. 29: Error terms for reflection probability.

An analytical expression for transmission probability (t) is given as:

$$t(r, L, S) = \text{logit}^{-1}(11.9368 - 0.17093 * Log(S) - 2.7043 * Log(L) - 9.5264 * r^{\frac{-1}{2}} - 6.86216 * L^{\frac{-1}{2}} + 0.05592 * Log(r) * Log(L) * Log(S)). \quad (147)$$

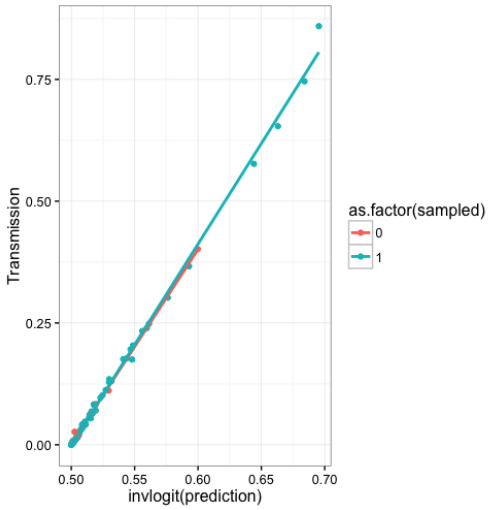

Fig. 30: Linear fit for actual and predicted transmission probability.

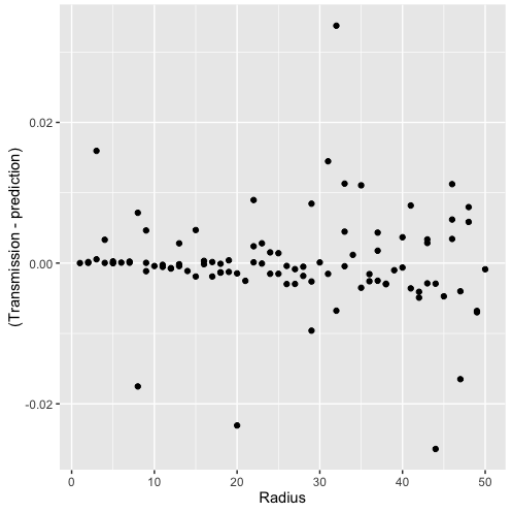

Fig. 31: Error terms for transmission probability.

A summary of the analytical expressions for concrete ducts can be seen below:

$$p_h(r, L, S) = \text{logit}^{-1}(0.8545 + 0.3919 * Log(S) - 0.2817 * Log(L * R) - 2.9212 * r^{\frac{-1}{2}} - 9.0932 * L^{\frac{-1}{2}}), \quad (148)$$

$$p_f(r, L, S) = \text{logit}^{-1}(-1.4733 + 0.9856 * Log(S) - 0.3947 * Log(L * R) - 3.4904 * r^{\frac{-1}{2}} - 12.1995 * L^{\frac{-1}{2}}), \quad (149)$$

$$t_h(r, L, S) = \text{logit}^{-1}(21.4706 - 2.07575 * Log(S) - 3.19662 * Log(L) + 0.07342 * Log(r) - 5.375 * r^{\frac{-1}{2}} - 10.1073 * L^{\frac{-1}{2}} - 17.0386 * S^{\frac{-1}{2}} + 0.0726 * Log(r) * Log(L) * Log(S)), \quad (150)$$

$$t_f(r, L, S) = \text{logit}^{-1}(11.1273 - 0.39242 * Log(S) - 2.73353 * Log(L) - 0.06618 * Log(r)$$
$$- 7.2351 * r^{\frac{-1}{2}} - 7.23506 * L^{\frac{-1}{2}} + 0.05254 * Log(r) * Log(L) * Log(S)). \quad (151)$$

Visualizations for reflection probability predictions, with respect to shield thickness, and transmission probability predictions, with respect to length, are provided for concrete ducts in Figs. 32-33. In each case, the predictions follow the general trend of the actual values (i.e. reflection probability increases as shielding thickness increases, and transmission probability decreases as length increases), but large errors can be observed; particularly in the case of reflection probability.

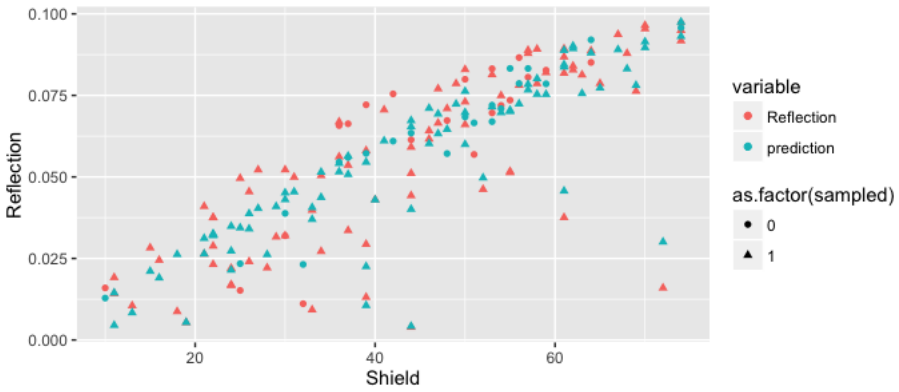

Fig. 32: Reflection probability predictions for concrete ducts, subject to a 14 MeV neutron source, with respect to shield.

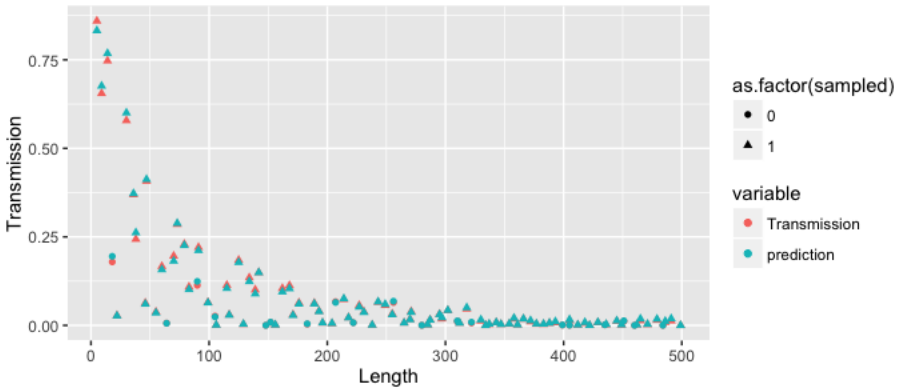

Fig. 33: Transmission probability predictions for concrete ducts, subject to a 14 MeV neutron source, with respect to length.

A summary of the analytical expression for iron (14 MeV source:f) and graphite (thermal:h) ducts:

$$p_{g/h}(r, L, S) = \text{logit}^{-1}(0.1993 + 0.8963 * Log(S) - 0.3698 * Log(L * R) - 3.1052 * r^{\frac{-1}{2}} - 12.1254 * L^{\frac{-1}{2}}), \quad (152)$$

$$p_{i/f}(r, L, S) = \text{logit}^{-1}(-0.8273 + 1.0253 * Log(S) - 0.3826 * Log(L * R) - 3.3089 * r^{\frac{-1}{2}} - 11.8660 * L^{\frac{-1}{2}}), \quad (153)$$

$$t_{g/h}(r, L, S) = \text{logit}^{-1}(16.58141 - 0.23959 * Log(S) - 3.2288 * Log(L) - 1.14356 * Log(r) - 11.9394 * r^{\frac{-1}{2}} - 10.09965 * L^{\frac{-1}{2}} - 0.07851 * Log(r) * Log(L) * Log(S)), \quad (154)$$

$$t_{i/f}(r, L, S) = \text{logit}^{-1}(12.883238 - 0.2033 * Log(S) - 2.94158 * Log(L) - 0.44419 * Log(r) - 8.71323 * r^{\frac{-1}{2}} - 9.03433 * L^{\frac{-1}{2}} + 0.06017 * Log(r) * Log(L) * Log(S)). \quad (155)$$

Tables XIX-XX provide summaries of average and median percent deviation for the training set ("Fit Avg./Median"), and the test set, for each material subject to a thermal source (h) and a 14 MeV source (f).

Table XIX: Percent difference for reflection probability of test set and fit.

Material	Fit Avg.	Test Avg.	Fit Median	Test Median
Iron(h)	5.14	6.07	2.48	2.55
Iron(f)	19.56	19.51	9.24	9.39
Concrete(h)	11.17	13.69	5.88	6.78
Concrete(f)	11.17	13.34	5.88	7.87
Graphite(h)	17.27	16.83	9.15	8.65
Graphite(f)	20.49	13.42	10.77	11.04

Table XX: Percent difference for transmission probability of test set and fit.

Material	Fit Avg.	Test Avg.	Fit Median	Test Median
Iron(h)	15.08	9.60	10.38	7.72
Iron(f)	16.24	14.62	10.35	10.86
Concrete(h)	19.90	19.95	10.95	10.95
Concrete(f)	19.90	14.07	10.95	8.01
Graphite(h)	21.53	20.16	12.05	10.90
Graphite(f)	15.42	13.82	9.39	7.15

IV.E. MCNP6 and Data Collection

Data is collected via MCNP6, [8] the general purpose Monte Carlo N-Particle code developed and maintained by Los Alamos National Laboratory, which is generally accepted as a benchmark for neutron, gamma, and electron transport calculations. For each of the geometric circular duct configurations a specifically tailored MCNP6 deck is created.

The duct system is defined within MCNP6 as two concentric cylinders, placed at the origin (0,0,0), with the length of the duct along the z-axis and the outer cylinder consisting of shielding material. An evacuated duct of radius r is defined as the inner cylinder, with a neutron source placed at the entrance of the duct. The thickness (in cm) of the shielding is defined as the length of the outer radius minus the length of the inner radius. The reflection and transmission probabilities are recorded via the F1 tally command, which is defined in MCNP as the number of particles crossing a surface in a given direction [8]

$$F1 = \int_A \int_\mu \int_t \int_E J(\hat{r}, E, t, \mu) dE dt d\mu dA, \tag{156}$$

where J is the surface current, t is time, E is energy of the particles, μ is the flight angle of particles, and A is the crossing area. Reflection probability is recorded as the net neutron current crossing the surface of the duct entrance, while transmission probability is a recorded as the same quantity at the duct exit. In order to ensure the the current is measured only at the duct entrance/exit (i.e. excluding any current crossing through the shielding material) we use a segmentation technique within the MCNP6 decks.

Given the large quantity of data collected (several hundred data points), the collection process was automated via codes written in the Python programming language and terminal shell scripts. Shell scripts (.sh) were used in the command terminal to automatically read MCNP6 decks into the TAMU nuclear engineering network (CLUSTER), initiate sequential MCNP6 runs, and then output result decks to a personal computer. Python scripts are used to manipulate parameters of an MCNP6 deck and write the adjusted deck to new files. Python scripts are also used to parse output files; that is, to read in reflection and transmission probability results into a csv file.

V. CONCLUSIONS

Reduced-physics (one-dimensional) and statistical models were developed as alternatives to computationally taxing three-dimensional, Monte Carlo and view factor codes. In this section, concluding remarks are provided for the reduced-physics and statstical models individually.

V.A. Nonlocal One-Dimensional Models

The problem of monoenergetic neutral particle transport in a duct is treated using an approximate one dimensional model for the third basis function, accounting for wall migration via a kernel density. Comparisons to MCNP results, furthermore, demonstrate that our one-dimension model performs well for iron and graphite ducts, while producing higher levels of error for concrete ducts. The higher error in concrete ducts may be attributed to a greater energy dependence, due to a large number of isotopes in the material, each with a distinct thermal neutron cross-section.

Garcia addresses the problem of energy-dependence by introducing a multi-group albedo approximation, where a value for wall reflection probability (c) is calculated for a number of subgroups in both the thermal and fast-range. The nonlocal one-dimensional models presented in this work, however, accounts only for one-speed neutrons (0.025 eV). Nonetheless, by accounting for wall migration the nonlocal one-dimensional models demonstrate significant improvement over the albedo approximation model for reflection probability, and comparable results for transmission probability. Direct comparisons between the models, for a thermal neutron source are provided in Tables XXI-XXII, where the nonlocal model is abbreviated as 1DWM,

and the albedo approximation model is abbreviated as 1DW/0. [6]

Table XXI: Reflection probability for ducts.

Material	1DWM Avg. %Dev.	1DW/O Avg. %Dev.	1DWM Max %Dev.	1DW/0 Max %Dev.
Iron	2.17	11.60	6.24	23.06
Concrete	13.57	56.69	21.22	105.3
Graphite	7.93	-	18.32	-

Table XXII: Transmission probability for ducts.

Material	1DWM Avg. %Dev.	1DW/O Avg. %Dev.	1DWM Max %Dev.	1DW/0 Max %Dev.
Iron	-7.58	-5.16	-9.98	-8.12
Concrete	-17.98	-6.21	-24.03	-11.91
Graphite	5.94	-	-7.94	-

A logical progression for the nonlocal one-dimensional model, therefore, would be to introduce a multigroup approach, where wall reflection probability (c) and the

average distance that particles migrate in walls (d) were calculated for a number of specified energy groups.

V.B. Multivariate Logistic Regression Model

Multivariate logistic regression models were developed, providing analytical expressions for the treatment of neutral particle transport in ducts with iron, graphite, and concrete shielding, for both thermal and fast neutron sources. While logistic regression models exhibit significant levels of error due to outliers, the median error is relatively low. In each case, the median prediction error falls under or only slightly above 10%.

Generally the model predictions for reflection probability are more accurate than the corresponding transmission probability (with the exception of graphite ducts with a 14 MeV neutron source). The median difference in accuracy can be explained by noting that for ducts of very large length, transmission probabilities are approximately zero; as such these values are difficult to capture, even for Monte Carlo codes. In general, however, there appears to be no consistent difference in prediction accuracy between models due to shielding material and energy source. In each case there exists a significant number of outliers, which can be attributed to a loss of information (i.e. the models cannot fully capture the physics of the system).

The logistic models presented in this work are intended for use with input values contained within the sample space; as such, the test sets used to evaluate the effectiveness of models for unseen data points all fall within the specified space. It should be noted, however, that the input ranges were quite broad, and chosen so at to coincide with duct dimensions that one can reasonably expect to see in ex-

periments and physical systems. Beyond the sample space, the models may entirely breakdown (though this is not guaranteed). For example, testing for the reflection and transmission probability in an iron duct system, subject to a thermal source, with semi-infinite shielding thickness, (specifically $S = 100$ cm + inner radius) and varying radius and length, the prediction % deviations can range from reasonably accurate to completely meaningless, as is seen in Tables XXIII - XXIV. Specifically the reflection probability predictions for random data points falling outside of the sample space, seen in Table XXIII, are fairly accurate with a median error of roughly 4 %; on the opposite extreme, the transmission probability predictions for random data points leads to a median error greater than 10^3, indicating a total breakdown of the model. The limitations of the transmission probability model, therefore, are well defined by the boundaries of the sample space.

Table XXIII: The predicted reflection probability for a random test set falling outside the sample space

Radius	Length	Shield	Actual	Predict.	%Dev.
10	40	110	0.1452	0.151	3.80
10	100	110	0.1696	0.153	10.87
25	50	125	0.1592	0.157	1.40
25	100	125	0.1762	0.169	4.28
25	150	125	0.1809	0.170	6.41
30	50	130	0.1587	0.153	3.76
50	550	150	0.1721	0.177	2.75
75	300	175	0.1721	0.178	3.27
75	350	175	0.1713	0.178	3.75
75	600	175	0.1661	0.179	7.18

Table XXIV: The predicted transmission probability for a random test set falling outside of the sample space.

Radius	Length	Shield	Actual	Predict.	%Dev.
10	40	110	0.07876	0.0103	664
10	100	110	0.01505	0.000791	1802
25	50	125	0.2701	0.0129	1994
25	100	125	0.1057	0.00388	2625
25	150	125	0.05423	0.00149	3539
30	50	130	0.3375	0.0135	2400
50	550	150	0.02334	0.000102	$> 10^4$
75	300	175	0.1362	0.001270	$> 10^4$
75	350	175	0.1092	0.000893	$> 10^4$
75	600	175	0.04744	0.000213	$> 10^4$

While the multivariate logistic regression models presented in this work produce a significant number of outliers, due to a loss of information, they produce reasonably accurate predictions within the sample space, and are therefore useful in instances where access to Monte Carlo codes is not possible, time constraints exist, or only estimates are required. In each case, the logistic regression models produces results instantly for large numbers of input values; that is, in a very small fraction of the time required for Monte Carlo simulations.

REFERENCES

[1] A.K. Prinja and G.C. Pomraning, "A Statistical Model of Transport in a Vacuum," *Transp. Theory Stat. Phys.* ,**13**, 567 (1984).

[2] E.W. Larsen, F. Malvagi, and G.C. Pomraning, "One-Dimensional Models for Neutral Particle Transport in Ducts," *Nuclear Science and Engineering*, **93**, 13 (1986).

[3] A.K. Prinja, "On the Solution of a Nonlocal Transport Equation by the Weiner-Hoff Method," *Ann. Nucl. Energy.* ,**23**, 429 (1996).

[4] R.D.M. Garcia, "The Third Basis Function Relevant to an Approximate Model of Neutral Particle Transport," *Nuclear Science and Engineering* ,**136**, 388 (2000).

[5] R.D.M. Garcia, "An Analytical Discrete-Ordinates Solution for an Improved One-Dimensional Model of Three-Dimensional Transport in Ducts," *Annals of Nuclear Energy*, **86**, 55 (2015).

[6] R.D.M. Garcia, S. Ono, W.J. Viera, "Approximate One-Dimensional Models for Multigroup Neutral-Particle Transport in Ducts," *Transp. Theory Stat. Phys.*, **32**, 505 (2003).

[7] J.F. Briesmeister, "MCNP- A General Monte Carlo N-Particle Transport Code, Version 6," LA- 12625 Ed., Los Alamos National Laboratory, Los Alamos, New Mexico (1997).

[8] R Core Team, "R: A language and environment for statistical computing," R Foundation for Statistical Computing, Vienna, Austria. (2013).

[9] Y. Jing, E.W. Larsen, and N. Xiang, "One-Dimensional Transport Equation Models for Sound Energy Propogation in Long Spaces: Theory," *J. Acoust. Soc. Am* , **127**, 2312 (2010).

[10] G.I. Bell and S. Glasstone, *Nuclear Reactor Theory*, Van Nostrand Reinhold, New York (1970)

[11] W.M. Stacey, *Nuclear Reactor Physics*, Wiley-VCH Verlag GmbH and Co. KGaA, New York (2007)

[12] T. Pang, *An Introduction to Computational Physics*, Cambridge University Press, Cambridge (1997)

[13] J.D. Hoffman, *Numerical Methods for Engineers and Scientists*, CRC Press, Boca Raton (2001)

[14] A. Gelman, J. Hill, *Data Analysis Using Regression and Multilevel/Hierarchical Models* , Cambridge University Press, Cambridge (2006).

[15] S.J. Sheather, *A Modern Approach to Regression with R*, Springer, New York (2009).

[16] D.G. Kleinbaum, M. Klein, *Logistic Regression: A Self-Learning Text*, Springer, New York (2010).

[17] V. Bewick, L. Cheek, J. Ball, "Statistics Review 14: Logistic Regression," *Critical Care* , **9**, 112 (205).

[18] P.J. Green, "Iteratively Reweighted Least Squares for Maximum Likelihood Estimation," *Journal of Royal Statistical Society*, **46**, 149 (1984).

[19] K.Q. Yeng, "Orthogonal Column Latin Hypercubes and their Application in Computer Experiments," *Journal of American Statistical Society*, **93**, 1430 (1998).